

1 **Holocene changes in deep-water circulation inferred from authigenic**  
2 **Nd and Hf isotopes in sediment records from the Chukchi-Alaskan**  
3 **and Canadian Beaufort margins**

4 Charles-Edouard Deschamps<sup>a,b,c,§</sup>, Jean-Carlos Montero-Serrano<sup>a,c,§,\*</sup>, Guillaume St-Onge<sup>a,b,c</sup>,  
5 André Poirier<sup>c</sup>

6  
7 <sup>a</sup>Institut des sciences de la mer de Rimouski, Université du Québec à Rimouski, Québec, Canada

8 <sup>b</sup>Canada Research Chair in Marine Geology, Institut des sciences de la mer de Rimouski,  
9 Université du Québec à Rimouski, Québec, Canada

10 <sup>c</sup>GEOTOP Research Center, Montréal, Québec, Canada

11 § Authors contributed equally

12 \*Corresponding author: J.-C. Montero-Serrano, E-mail address: [jeancarlos\\_monteroserrano@uqar.ca](mailto:jeancarlos_monteroserrano@uqar.ca).

13  
14 **Key points**

15 1. The first authigenic Nd and Hf isotope records in Holocene sediment cores from the Canadian  
16 Beaufort and Chukchi-Alaskan margins are presented.

17 2. Unradiogenic Nd-Hf isotopic values between 11 and 4 ka cal BP are due to major weathering  
18 in the drainage basin of the Yukon/Mackenzie Rivers.

19 3. Radiogenic Nd-Hf isotopic compositions after 4 ka cal BP reveal an increase in the  
20 Atlantic/Pacific water inflows through the Arctic Ocean.

21

22

23 **Abstract**

24         The rare earth element (REE) concentrations and radiogenic isotope (Sr-Nd-Hf)  
25 compositions measured in bulk sediment leachates, together with bulk and clay mineralogical  
26 data, from two piston cores recovered in the Canadian Beaufort (AMD0214-02PC) and Chukchi-  
27 Alaskan (HLY0501-01JPC) margins were studied to investigate changes in the weathering  
28 regimes and deep-water circulation during the Holocene. The coupled evolutions of the Nd and  
29 Hf isotopic compositions (expressed in epsilon units:  $\epsilon\text{Nd}$  and  $\epsilon\text{Hf}$ , respectively) are in good  
30 agreement with modern seawater and bulk sediment leachate data from Pacific water, Atlantic  
31 water and the Mackenzie River. This agreement supports the idea that boundary exchange and  
32 brine formation likely play a significant role in the  $\epsilon\text{Nd}$  and  $\epsilon\text{Hf}$  values of the bottom waters in  
33 the western Arctic Ocean. The  $\epsilon\text{Nd}$  and  $\epsilon\text{Hf}$  records from the Canadian Beaufort and Chukchi-  
34 Alaskan margins reveal changes towards more radiogenic values from the early to late Holocene.  
35 Based on the  $\epsilon\text{Nd}$  and  $\epsilon\text{Hf}$  records, we suggest that the unradiogenic values are not controlled by  
36 water mass provenance and mixing but rather by provenance and a change in the weathering  
37 regime in the Mackenzie and Yukon drainage basins during the early to mid-Holocene. In  
38 contrast, the more radiogenic  $\epsilon\text{Nd}$  and  $\epsilon\text{Hf}$  values in the Chukchi-Alaskan margin and the  
39 mineralogical records in the late Holocene have primarily been controlled by an increase in the  
40 contributions of seawater and detrital particles from the Bering Sea via the Bering Strait inflow,  
41 which is likely related to major changes in the Pacific Ocean–atmospheric dynamics.

42

43 **Keywords:** Canadian Beaufort Sea; Chukchi Sea; REE distribution; neodymium isotopes;  
44 hafnium isotopes; mineralogy; sediment; Fe-Mn oxyhydroxides; Holocene; deglaciation.

## 45 **1 Introduction**

46           The Arctic Ocean plays an important role in regulating Earth's climate because (1) its  
47 perennial sea ice cover modulates the atmospheric and oceanic heat budget since it reflects a  
48 large part of the incoming solar radiation during the summer (albedo) and acts as an insulating  
49 shield during the winter (Serreze et al., 2007) and (2) the export of freshwater into the North  
50 Atlantic affects the Atlantic meridional overturning circulation by changing the deep-water  
51 convection (Dickson et al., 2007). The northward flows of Atlantic and Pacific waters  
52 (hereinafter referred to as AW and PW, respectively) are the major sources of heat advection  
53 towards the Arctic Ocean and strongly affect sea ice distribution (Kinnard et al., 2011; Polyakov  
54 et al., 2017). For example, the increase in warm AW to the Arctic over the past 2,000 years seems  
55 to be the main factor in sea ice decline (Kinnard et al., 2011). Likewise, the advection of warm  
56 PW into the Arctic Ocean induces a greater supply of heat in the western Arctic Ocean and acts  
57 as a trigger for sea ice decline in the Chukchi Sea (Shimada et al., 2006; Stein et al., 2017). In this  
58 context, paleoceanographic and paleoclimate proxy records from marine sediment cores can  
59 provide evidence for the large-scale natural variability in the Arctic deep-water circulation during  
60 the late Quaternary, against which recent changes can be compared. A better understanding of the  
61 past variation in the deep-water circulation may help to decipher the processes controlling Arctic  
62 climate and sea ice variability.

63           The neodymium (Nd) and hafnium (Hf) isotope compositions of rocks largely depend on  
64 the lithology and crustal age. The Nd and Hf isotope compositions are denoted in epsilon units  
65 ( $\epsilon\text{Nd}$  and  $\epsilon\text{Hf}$ ), which reflect the normalization of the  $^{143}\text{Nd}/^{144}\text{Nd}$  and  $^{176}\text{Hf}/^{177}\text{Hf}$  ratios to the  
66 chondritic uniform reservoir (Jacobsen and Wasserburg, 1980; Nowell et al., 1998). Hence, low  
67  $^{143}\text{Nd}/^{144}\text{Nd}$  values ( $\epsilon\text{Nd}$  of -40) reflect old continental crust, while high  $^{143}\text{Nd}/^{144}\text{Nd}$  values ( $\epsilon\text{Nd}$

68 of +20) reflect young mantle-derived rocks (Frank, 2002). The variability in the Hf isotope  
69 composition in terrestrial rocks is larger than that in Nd, ranging from the most unradiogenic  
70 values of  $\epsilon_{\text{Hf}} \sim -50$  in Archean rocks to values as high as +25 in mid-ocean ridge basalt  
71 (Zimmermann et al., 2009a). Water masses from different origins therefore acquire distinct  
72 regional  $\epsilon_{\text{Nd}}$  and  $\epsilon_{\text{Hf}}$  signatures derived primarily from riverine continental input, particle-  
73 dissolved exchange processes (a process commonly referred to as boundary exchange) and/or  
74 benthic sources (e.g., Frank, 2002; Jeandel et al., 2007; Rickli et al., 2009; Zimmermann et al.,  
75 2009a,b; Wilson et al., 2013; Abbott et al., 2016; Haley et al., 2017). Consequently, Nd and Hf  
76 can be used as sensitive tracers for both (1) water mass mixing and provenance (Chen et al.,  
77 2012; Rickli et al., 2009; Stichel et al., 2012), because both elements' oceanic residence times are  
78 shorter than the oceanic mixing time (approximately 1500 yr; Frank, 2002), and (2) detrital  
79 provenance changes and continental weathering intensity (Gutjahr et al., 2014; Rickli et al.,  
80 2010). Because dissolved trace elements are incorporated by coprecipitation processes during  
81 early burial in the top few centimeters of the sediments (Bayon et al., 2004; Haley et al., 2004),  
82 the authigenic Nd and Hf signatures can be extracted from ferromanganese (Fe–Mn)  
83 oxyhydroxide coatings on marine sediment samples (Bayon et al., 2004; Gutjahr et al., 2007;  
84 Chen et al., 2012). Based on these findings, the analysis of  $\epsilon_{\text{Nd}}$  and  $\epsilon_{\text{Hf}}$  signatures of authigenic  
85 fractions in marine sediments is a powerful tool for assessing late Quaternary changes in water  
86 mass provenance and in pathways of weathering inputs.

87         Taking this into account, a number of studies have investigated the seawater Nd and Hf  
88 isotope compositions of past Arctic Intermediate Water extracted from the authigenic Fe–Mn  
89 oxyhydroxide fraction of late Tertiary (mid-Miocene) to Quaternary sedimentary records to  
90 decipher changes in the weathering regimes and water mass mixing (e.g., Haley et al., 2008;  
91 Horikawa et al., 2015; Chen et al., 2012; Maccali et al., 2013; Meinhardt et al., 2016a; Jang et al.,

92 2017). Likewise, modern Nd and Hf isotope compositions of seawater in Arctic Ocean basins  
93 (Porcelli et al., 2009; Zimmermann et al., 2009a) and pre-modern authigenic Nd isotope  
94 signatures of surface sediments from the Arctic Ocean seafloor (Haley & Polyak, 2013) have  
95 been investigated to better present the Arctic Ocean's circulation patterns. Nonetheless, the  
96 Holocene variability in the contributions of different water masses to the deeper parts of the  
97 western Arctic Ocean is not yet completely understood. Thus, authigenic Nd and Hf isotopic  
98 compositions retrieved from sediment cores may provide new clues concerning the evolution of  
99 the Holocene deep circulation and climate in the western Arctic Ocean, which may then help to  
100 place modern environmental changes in perspective.

101 In this context, the Nd and Hf isotope signatures and the rare earth element (REE)  
102 concentrations obtained from the authigenic Fe–Mn oxyhydroxide fractions, together with the  
103 bulk and clay mineralogical analysis, of two sediment piston cores recovered from the Chukchi-  
104 Alaskan (core HLY0501-01JPC) and Canadian Beaufort (core AMD0214-02PC) margins are  
105 used here to (1) assess changes in the provenance of deep-water masses, (2) interpret variations in  
106 the dynamics of deep-water circulation in terms of paleoenvironmental changes since the last  
107 deglaciation, and (3) provide new insights into the potential relationships between changes in  
108 erosional inputs and oceanic circulation variations in the western Arctic Ocean since the last  
109 deglaciation.

## 110 **2 Regional setting**

### 111 **2.1. Oceanic circulation**

112 The Arctic surface oceanic circulation is related to two main wind-driven circulation  
113 systems, which are the anticyclonic Beaufort Gyre (BG) in the western Arctic and the Transpolar  
114 Drift (TPD; Darby & Bischof, 2004). On the Beaufort Shelf, the anticyclonic BG pushes both

115 surface currents and sea ice westward at the shelf break. Conversely, closer to shore around the  
116 50-m isobath, the Beaufort Undercurrent transports both PW and AW eastward along the  
117 continental margin and into the Amundsen Gulf (Forest et al., 2011). The AW flows through the  
118 Fram Strait and the Barents Sea. The depth of the AW is between 200 and 1000 m and has a  
119 temperature above 0 °C (Rudels et al., 2004). The AW circulation is counterclockwise along the  
120 margins of the Arctic Ocean. It begins along the Eurasian margin and then separates at the level  
121 of the Lomonosov Ridge. A branch of the AW circulation diverges towards the eastern face of  
122 the Lomonosov Ridge, and the other branch continues in the Canadian basin (Figure 1; Poirier et  
123 al., 2012). The modern Nd and Hf isotope signatures of the AW in Arctic Ocean basins have been  
124 studied in Porcelli et al. (2009) and Zimmermann et al. (2009a), and the results showed  $\epsilon_{\text{Nd}}$  and  
125  $\epsilon_{\text{Hf}}$  values of -9 and 1.6, respectively.

126         The Chukchi Shelf circulation is controlled by an inflow of PW via the Bering Strait  
127 (referred to as the Bering Strait inflow or BSI), the Siberian coastal current, and the Atlantic  
128 Intermediate Water affecting the northern margin (Figure 1a; Pickart, 2004; Weingartner et al.,  
129 2005). PW from the Bering Sea flows into the Chukchi Sea in three major branches (Figure 1a;  
130 Pickart et al., 2004, 2005; Weingartner et al., 2005; Grebmeier et al., 2006; Okkonen et al., 2009;  
131 Danielson et al., 2014; Corlett & Pickart, 2017). The first branch, composed of cold, salty (>32.5)  
132 and nutrient-rich Anadyr Water, flows through Hope Valley into Herald Canyon. The third  
133 branch, composed of warm, fresh (<31.8) and nutrient-poor Alaskan Coastal Water, flows into  
134 Barrow Canyon following the northwestern Alaskan coast in the eastern Chukchi Sea (known as  
135 the Alaska Coastal Current). The second branch, composed of intermediate saline (31.8–32.5)  
136 and lower nutrient Bering Shelf Water, flows between the first and the third branches through the  
137 Central Channel. In general, within the Chukchi Sea, the Anadyr and Bering Shelf waters are  
138 both named Bering Sea Water (e.g., Grebmeier et al., 2006; Stein et al., 2017). At interannual

139 time scales, the intensity of the BSI is controlled mainly by the Aleutian Low pressure center's  
140 strength and position (Yamamoto et al., 2017). Periods of strengthening of the Aleutian Low  
141 pressure center, located over the eastern North Pacific, induce a decrease in the BSI into the  
142 Arctic Ocean (Danielson et al., 2014). According to modern hydrographic observations, dense  
143 waters (brines) generated at the Chukchi-Alaskan margin during fall/winter sea ice formation can  
144 descend to a pycnocline depth of up to 200 m (Pickart et al., 2005; Woodgate et al., 2005).  
145 Corlett & Pickart (2017) have shown that PW flows into the Barrow Canyon and forms a slope  
146 current called the Chukchi Slope current. The Chukchi Slope current can transport 0.50 Sv of PW  
147 westward of Barrow Canyon and can extend into the Atlantic layer (Corlett & Pickart, 2017). The  
148 isotopic signature of the PW before entering the Chukchi Sea has been described in Zimmermann  
149 et al. (2009b) and Asahara et al. (2012), with  $\epsilon\text{Nd}$  values of approximately -2 to -3 and  $\epsilon\text{Hf}$  values  
150 ranging from 3.5 to 8.6 with a mean value of 6.8. The isotopic signature of the PW throughflow  
151 water in the Chukchi Sea is  $\epsilon\text{Nd} = -5$  and  $\epsilon\text{Hf} = 5.8$  (Haley & Polyak, 2013; Porcelli et al., 2009;  
152 Zimmermann et al., 2009a). The change in terms of the isotopic signature of the PW before and  
153 after the Bering Strait is possibly due to the influence of runoff from the Yukon and Anadyr  
154 rivers and/or so-called boundary exchange with northeastern Bering Sea sediments (Haley &  
155 Polyak, 2013; Porcelli et al., 2009). The  $\epsilon\text{Nd}$  signature of the Yukon River is  $\epsilon\text{Nd} = -8$  to -9  
156 (VanLaningham et al., 2009), and the Hf isotopic signature is still unknown (Horikawa et al.,  
157 2010). An increase in the BSI into the Chukchi Sea generally leads to reduced sea ice cover and  
158 an increase in sea surface temperature (e.g., McKay et al., 2008; Polyak et al., 2016; Stein et al.,  
159 2017). However, as the BSI flows into the Chukchi Sea in three main branches (Figure 1a), the  
160 sea ice cover in this region show considerable spatial and temporal variability (Polyak et al.,  
161 2016).

162

## 163 **2.2. Sedimentation**

164 On the Canadian Beaufort Shelf and the Chukchi Sea, most of the surficial seabed sediments  
165 are predominantly composed of Holocene bioturbated gray to olive-gray marine silts and clays  
166 (Gamboa et al., 2017; Kobayashi et al., 2016). The modern sedimentation in the Chukchi Sea is  
167 believed to be mainly derived from northeastern Siberia, the northeastern Bering Sea (mainly  
168 from the Yukon River and to lesser extents from the Aleutian arc and Anadyr River) and the  
169 Mackenzie River, whereas the Canadian Beaufort margin sediment originates primarily from the  
170 Mackenzie River basin (Nelson and Creager, 1977; Darby et al., 2011; Asahara et al., 2012;  
171 Horikawa et al., 2015; Kobayashi et al., 2016; Gamboa et al., 2017; Deschamps et al., 2018a).  
172 Smaller Alaskan rivers have a more local impact but may have been a more important sediment  
173 source during the early stages of the last transgression (Hill & Driscoll, 2008). During  
174 deglaciation and the early Holocene, sediment inputs to the Chukchi-Alaskan and Beaufort  
175 margins were presumably higher due to the rising sea level associated with meltwater and iceberg  
176 discharge from the retreat of large ice sheets (Deschamps et al., 2018a).

## 177 **3 Material and methods**

### 178 **3.1 Sample and chronology**

179 The sediment core HLY0501-01JPC (hereinafter referred to as core 01JPC; water depth:  
180 1163 m; location: 72°90'N, 158°42'W) was recovered at the Chukchi-Alaskan margin on board  
181 the USCGC Healy as part of the 2005 Healy-Oden Trans-Arctic Expedition (Figure 1a,b). Core  
182 AMD0214-02PC (hereinafter referred as core 02PC; water depth: 998 m; location: 71°22.910'N,  
183 133°34.040'W) was collected on the Canadian Beaufort margin on board the CCGS Amundsen  
184 during the 2014 ArcticNet expedition (Figure 1a,b). Age models and physical properties of the

185 01JPC and 02PC sediment cores have been described in Deschamps et al. (2018b). The  
186 authigenic Fe–Mn oxyhydroxide coatings preserved within these sediment cores likely records  
187 past bottom water REE signatures, as reductive diagenesis processes is seem to be negligible  
188 (Figure S1; Deschamps et al., 2018b). The sedimentation rate for core 02PC ranged from 2-20  
189  $\text{cm.k}^{-1}$  in the postglacial units, whereas the sedimentation rate in core 01JPC is constant in the  
190 postglacial unit ( $60 \text{ cm.k}^{-1}$ ). Core 01JPC is characterized by a hiatus in the sedimentary  
191 sequence at approximately 6 ka cal BP and the deglacial section of the core (Deschamps et al.,  
192 2018b). For this reason, only the Holocene units of core 01JPC have been sampled ( $n=11$ ,  
193 resolution of 500 years). Core 02PC spans the last 13.5 ka cal BP and is characterized by two ice-  
194 rafted debris (IRD) intervals between 140 and 160 cm (IRD1) and 320 and 360 cm (IRD2)  
195 (Deschamps et al., 2018b). In this study, we focus on the last 11.5 ka cal BP ( $n= 22$ , resolution of  
196 500 years).

197

## 198 **3.2 Radiogenic isotopes and REE analyses**

### 199 **3.2.1 Bulk sediment leaching**

200 Seawater Sr, Nd and Hf isotopic signatures from authigenic Fe-Mn coatings of the bulk  
201 sediment were extracted applying the leaching protocol of Chen et al. (2012). Briefly, 1 g of dried  
202 and powdered sediments was rinsed three times with Milli-Q water. Next, Sr, Nd and Hf  
203 contained in the sediment oxyhydroxide fraction were leached for approximately 1 h in a single  
204 step using a dilute reducing and complexing solution consisting of 0.005 M hydroxylamine  
205 hydrochloride (HH), 1.5% acetic acid, and 0.03 M Na-EDTA, buffered to  $\text{pH} = 4$  with suprapur®  
206 NaOH. A buffered acetic acid leach step was omitted since biogenic carbonates are negligible in  
207 all sediment samples (Deschamps et al., 2018a). The hydroxylamine hydrochloride and acetic

208 acid mixture was 10-fold diluted compared with the method of Gutjahr et al. (2007) to avoid any  
209 potential contamination caused by the leaching of clay minerals. During treatment, the sediment  
210 samples were gently shaken to enhance the reaction. Leaching method was applied on two  
211 sediments sample, one for the REE concentration analyses and the other one for the Nd and Sr  
212 chromatographic extraction. The aliquot for REE concentration analysis was evaporated almost  
213 to dryness and the residue was re-dissolved in 1 mL of concentrated HNO<sub>3</sub> and subsequently  
214 diluted with Milli-Q water to a total volume of 5 mL.

215

### 216 **3.2.2 Sr, Nd and Hf separation: column chemistry**

217 The Sr, Nd and Hf were separated from the other elements by applying a single-step ion  
218 chromatographic separation (Li et al., 2014). Briefly, the leaching solutions obtained from the  
219 previous steps were centrifuged at 5000 rpm for 8 min. Then, 1 mL of the supernatant solution  
220 was passed through a two-layered mixed resin column (70 mm length, 6 mm diameter) with the  
221 upper layer containing 1.5 mL of Biorad® AG50W-X12 (200–400 mesh) resin and the bottom  
222 layer containing 0.45 mL of Eichrom® LN Spec resin (100–150 µm). Before sample loading for  
223 the separation of Sr–Nd–Hf from the sample matrix, the mixed resin column was pre-washed  
224 with 18 mL of 6 M HCl, 8 mL of 3 M HF, and 4 mL of H<sub>2</sub>O in turn. After sample loading and  
225 rinsing four times with 0.5 mL of 2.5 M HCl, the column was washed with 13.5 mL of 2.5 M  
226 HCl. Most matrix elements (K, Ca, Na, Mg, Al, Fe, Mn, Ti) and Rb were removed during this  
227 step. Then, the Sr fraction was stripped with 5.5 mL of 2.5 M HCl. Part of the HREE (Dy, Ho,  
228 Er, Tm, Yb, Lu) and Ba were then washed out with 3 mL of 2.5 M HCl. Next, the Nd was then  
229 isolated from the other REE with 8 mL of 6 M HCl. Finally, the Hf was isolated with 5 mL of 3  
230 M Hf. Then, the Sr, Nd, and Hf fractions were dried on a hotplate at 120°C to dryness and

231 prepared for isotope measurements.

### 232 **3.2.3 REE concentrations and Sr-Nd-Hf analysis**

233 The REE concentrations (La, Ce, Pr, Nd, Sm, Eu, Gd, Tb, Dy, Ho, Er, Tm, Yb and Lu)  
234 were determined using an inductively coupled plasma-quadrupole mass spectrometer (ICP-QMS  
235 Agilent 7500c) at ISMER. Procedural blanks (chemistry and mass spectrometry) always  
236 accounted for less than 1% of the lowest concentrations measured in the samples. Multi-element  
237 stock standard solution containing all REE (multi-element solution 1, CLMS-1, Spex Certiprep  
238 Inc., Quebec, Canada) was used to prepare external calibration and a quality control standard  
239 solution containing 4 ng/mL of each REE. ICP-QMS external reproducibility, based on replicate  
240 analysis of this control standard solution, was <11% relative standard deviation (RSD,  $1\sigma$ ) for all  
241 REE. The REE abundances were normalized to Post-Archean Australian Shale (PAAS; Taylor &  
242 McClennan, 1985) in order to evaluate the REE patterns as given in (Maccali et al., 2013) and Du  
243 et al. (2016). The fractionation between the light REE (LREE: La–Nd), medium REE (MREE:  
244 Sm–Dy) and heavy REE (HREE: Tm–Lu) was investigated using the following indices:  
245 HREE/LREE ( $[\text{Yb} + \text{Lu}]/[\text{Pr} + \text{Nd}]$ ) and MREE\* ( $2[\text{Tb} + \text{Dy}]/[\text{Pr} + \text{Nd} + \text{Yb} + \text{Lu}]$ ) to investigate  
246 the fractionation between LREE, MREE, and HREE (Du et al., 2016; Molina-Kescher et al.,  
247 2014).

248 The Sr isotopic ratios ( $^{88}\text{Sr}/^{86}\text{Sr}$ ) were measured in dynamic mode on a Thermo Scientific  
249 Triton Plus™ multicollector thermal ionization mass spectrometer (TIMS) at GEOTOP  
250 (Montreal, Canada). The Sr samples were loaded and analyzed on a single outgassed zone-refined  
251 Re filament, layered with a tantalum activator solution (Birck, 1986). Repeated analyses of the  
252 NIST-987 standard (n=6) yielded values of 0.710276 ( $\pm 0.000021$ ,  $2\sigma$  reproducibility). This mean  
253 value compares well to its certified value of 0.710248 (Weis et al., 2006). The total procedural

254 blanks for Sr were less than 0.5 ng, which is considered negligible compared to the sample yields  
255 (> 100 ng).

256 The Nd and Hf isotopic ratios ( $^{143}\text{Nd}/^{144}\text{Nd}$  and  $^{176}\text{Hf}/^{177}\text{Hf}$ ) were analyzed on a Nu  
257 Plasma II instrument, a Multi-Collector Inductively Coupled Plasma Mass Spectrometer (MC-  
258 ICP-MS), also at GEOTOP, in “dry-plasma” conditions using an Aridus II desolvating  
259 membrane as the introduction device. The mass-bias correction was made by monitoring  
260  $^{146}\text{Nd}/^{144}\text{Nd}$  (taken to be equal to 0.7219) and  $^{176}\text{Hf}/^{177}\text{Hf}$  (taken to be equal to 0.7325) and by  
261 applying an exponential beta-factor correction to the other ratios. Replicate analyses of the  
262 standard JNdi-1 and JMC 475 yielded a mean value of  $^{143}\text{Nd}/^{144}\text{Nd} = 0.512108 \pm 0.000020$  ( $2\sigma$ ;  
263  $n=20$ ) and  $^{176}\text{Hf}/^{177}\text{Hf} = 0.282159 \pm 0.000009$  ( $2\sigma$ ;  $n=20$ ) which are within the uncertainty of its  
264 certified values of  $0.512115 \pm 0.000007$  (Tanaka et al., 2000) and  $0.282160 \pm 0.000032$  (Nowell et  
265 al., 1998), respectively. Hence, no correction has been applied to the Nd and Hf isotope data. The  
266 external reproducibility was provided by the repeated measurements of the JNdi-1 (from 0.1 to  
267 0.3  $\epsilon$  units,  $2\sigma$ ;  $n=31$ ) and JMC 475 (0.5 to 1.3  $\epsilon$  units,  $2\sigma$ ;  $n=31$ ) standards at the same  
268 concentration as the samples. Thus, the analytical error for each sample analysis is taken as the  
269 external reproducibility of the JNdi-1 and JMC 475 standard in each analytical session. Some  
270 samples have higher uncertainties (up to 0.4  $\epsilon$  units for Nd and up to 9  $\epsilon$  units for Hf; Table S2)  
271 because of poorer counting statistics of samples with low Nd and Hf concentrations. The  
272 procedural blank values were < 0.5 ng for Nd and for Hf and were therefore neglected as they  
273 represented less than 0.1% of the Nd and Hf analyzed per sample, respectively. The  $^{143}\text{Nd}/^{144}\text{Nd}$   
274 and  $^{176}\text{Hf}/^{177}\text{Hf}$  isotopic ratios are expressed in  $\epsilon$  units ( $\epsilon\text{Nd}$  and  $\epsilon\text{Hf}$ ).

### 275 **3.3 Bulk and clay mineralogical analyses**

276 Complementary bulk mineral associations were studied by quantitative X-ray diffraction  
277 (qXRD) following the method developed by Eberl (2003). Briefly, ~1 g of each sample was  
278 spiked with 0.25 g of corundum, and the powder samples were scanned from 5° to 65° two-theta  
279 in steps of 0.02° two-theta on a PANalytical X'Pert Powder diffractometer. For the quantification  
280 of the major mineralogical components, sediment XRD scans obtained were converted into  
281 mineral weight percent (wt. %) using the Excel macro program ROCKJOCK v11 (Eberl, 2003).  
282 Then, we used the non-linear unmixing Excel macro program SedUnMixMC (Andrews & Eberl,  
283 2012) to gain a quantitative understanding of the downcore changes in bulk sediment provenance.  
284 In addition, clay mineral associations were studied using XRD following established protocols  
285 (Bout-Roumazelles et al., 1999). The separated clay-sized fraction was concentrated by  
286 centrifugation and oriented by wet smearing on glass slides. The analyses were run from 2.49° to  
287 32.49° two-theta on a PANalytical X'Pert Powder diffractometer. Three X-ray diagrams were  
288 performed, and after the sample was air-dried, ethylene glycol vapor saturation was completed  
289 for 12 h, followed by heating at 490 °C for 2 h. A semi-quantitative estimation of clay mineral  
290 abundances (smectite, illite, chlorite, kaolinite, vermiculite and a chlorite/smectite mixed layer)  
291 based on peak areas was performed using the MacDiff® 4.2.5 software (Petschick, 2000). Similar  
292 to other Arctic clay mineral studies (Schoster et al., 2000; Wahsner et al., 1999), the clay mineral  
293 contents were calculated by using the weighting factors introduced by Biscaye (1965) and  
294 calculated to a sum of 100%. Note that bulk and clay mineralogical analyses on sediments for the  
295 core 02PC were reported previously (Deschamps et al., 2018a). In this study, based on a previous  
296 sediment provenance study in the western Arctic Ocean (Deschamps et al., 2018a), we used the  
297 proportion of sediments derived from the Bering Strait and Mackenzie River (SedUnMixMC

298 results), as well as the amorphous silica contents and  $\text{Log}(\text{illite}+\text{kaolinite}/\text{chlorite}+\text{vermiculite})$   
299 ratio or  $\text{Log}(\text{I}+\text{K}/\text{C}+\text{V})$  to trace sediment provenance changes over time. The high amorphous  
300 silica concentrations in the Chukchi Sea sediments can be interpreted as a major inflow of  
301 biosilica-rich PW through the Bering Strait (Jakobsson et al., 2017; Stein et al., 2017). Likewise,  
302 the  $\text{Log}(\text{I}+\text{K}/\text{C}+\text{V})$  ratio allowed us to discriminate between sediments from the Bering Strait  
303 (rich in chlorite and vermiculite) and sediments from the Mackenzie River (rich in illite and  
304 kaolinite).

## 305 **4 Results**

### 306 **4.1 Authigenic REE distribution**

307 The REE concentrations are presented in Table S1. The PAAS-normalized REE of the bulk  
308 sediment leachates from both cores reveal an MREE bulge-type pattern (Figure 2), with an  
309 enrichment in MREEs compared to HREE and LREE, which is a common pattern in leachates  
310 and authigenic material (Gutjahr et al., 2007; Du et al., 2016; Abbott et al., 2016). Likewise, to  
311 further evaluate the efficiency of our procedure for extracting the authigenic phase, we compared  
312 the HREE/LREE ratios to the MREE\* values (Figure 3b). The HREE/LREE-MREE\* cross-plots  
313 reveal that all our bulk sediment leachates plot on the Fe–Mn leachate array (Du et al., 2016;  
314 Gutjahr et al., 2010). This finding indicates that authigenic Fe–Mn oxyhydroxide coatings control  
315 the Nd and Hf signals in our bulk sediment leachates. Furthermore, the significant negative  
316 correlation observed between the  $\Sigma\text{REE}$  content and  $\epsilon\text{Nd}$  values in cores 01JPC ( $r = -0.75$ ) and  
317 02PC ( $r = -0.59$ ) suggests  $\Sigma\text{REE}$  enrichment towards more unradiogenic values (Figures 3b).

## 318 **4.2 Sr, Nd and Hf isotope signatures**

319 The Sr, Nd, and Hf isotope data obtained from the leachates are provided in Table S2. The  
320  $^{87}\text{Sr}/^{86}\text{Sr}$  values obtained from the bulk sediment leachates in cores 01JPC and 02PC range from  
321 0.70922 to 0.70940, with a mean value of  $0.70929 \pm 0.00004$  (Figure 3a). These values are  
322 characteristic of the present-day sea water values recorded in the western Arctic Ocean (0.70920;  
323 Asahara et al., 2012). In core 01JPC, the  $\epsilon\text{Nd}$  values range from -3.7 to -5.7, while the  $\epsilon\text{Hf}$  values  
324 range from 4.1 to 9.2 (Figures 3d and 4a). In general, the Nd and Hf isotopic signatures in core  
325 02PC are less radiogenic than those in core 01JPC. The  $\epsilon\text{Nd}$  values range from -7.6 to -16.8,  
326 while the  $\epsilon\text{Hf}$  values range from 4.8 to -10.4 (Figures 3d and 4b,c). As shown in Figure 3d, the  
327 Nd-Hf isotope values of core 01JPC fall into the sea water array, whereas the data from core  
328 02PC range from the sea water array to the detrital array.

## 329 **4.3 Bulk and clay mineralogical data**

330 The stratigraphic distributions of the bulk and clay mineralogical data from core 02PC are  
331 shown in Deschamps et al. (2018a). The mineralogy of the bulk sediment fraction of core 02PC is  
332 dominated by quartz (~22%) and total clays (72%). The clay mineral assemblage of core 01JPC  
333 consists of illite (60%), kaolinite (14%), chlorite (14%), vermiculite (8%) and mixed-layer  
334 chlorite/smectite (2%). Based on the SedUnMixMC results (Figure 5g), the major source of  
335 sediment for core 02PC is related to the Mackenzie River (> 80%), and the secondary source is  
336 the Canadian Arctic Archipelago (up to 60%). The bulk and clay minerals concentrations of the  
337 core 01JPC are presented in Tables S3 and S4, respectively. The mineralogy of the bulk sediment  
338 fraction of core 01JPC is dominated by quartz (~20%), total clays (52%), plagioclase (11%), K-  
339 feldspar (5%) and amorphous silica (3-14%), and the clay mineral assemblage of core 01JPC  
340 consists of illite (27-45%), kaolinite (5-10%), chlorite (10-15%), vermiculite (7-50%) and mixed-

341 layer chlorite/smectite (0-40%). Based on the SedUnMixMC results (Figure 6f; Table S5), the  
342 major source of sediment for core 01JPC is related to the northeastern Bering Sea (40-60%), and  
343 the secondary source is the Mackenzie River (10-30%).

## 344 **5 Discussion**

### 345 **5.1 Nd and Hf isotopic compositions of cores 02PC and 01JPC**

346 As shown in Figures 3d and 4b,c, the Nd and Hf isotopic composition of core 02PC  
347 displays high variations and ranges between the signatures of the AW ( $\epsilon_{\text{Nd}}$ : -9,  $\epsilon_{\text{Hf}}$ : 1.6;  
348 Zimmermann et al., 2009a) and the modern Mackenzie River ( $\epsilon_{\text{Nd}}$ : -12.9,  $\epsilon_{\text{Hf}}$ : -7.1;  
349 Zimmermann et al., 2009a). From 12 to 6 ka cal BP, the  $\epsilon_{\text{Nd}}$  values in core 02PC are clearly  
350 similar to those of the Mackenzie River, whereas between 6 and 2 ka cal BP, the Nd isotopic  
351 values become more radiogenic and reflect a mixture between those of the AW and the  
352 Mackenzie River (Figure 4b,c). After 2 ka cal BP, the  $\epsilon_{\text{Nd}}$  values match those of the AW. Similar  
353 to the Nd isotopic compositions, the  $\epsilon_{\text{Hf}}$  isotopic values in core 02PC transition from a clear  
354 Mackenzie River signature (12-6 ka cal BP) to a mixed signature between the Mackenzie River  
355 and the AW (6-2 ka cal BP) to predominantly an AW signature after 2 ka cal BP (Figure 4b,c).

356 As shown in Figures 3d and 4a, the Nd isotopic values of core 01JPC between 6 and 4 ka  
357 cal BP ( $\epsilon_{\text{Nd}} \sim -5.5$ ) are very similar to those of the PW recorded in the Chukchi Sea region  
358 (Haley & Polyak 2013; Zimmermann et al., 2009a). This  $\epsilon_{\text{Nd}}$  signature likely represents a  
359 mixture dominated mainly by unradiogenic Nd isotope compositions from the Yukon River ( $\epsilon_{\text{Nd}}$   
360  $\sim -8$  to  $-9$ ) and a minor proportion of more radiogenic Nd isotope compositions from the Aleutian  
361 arc ( $\epsilon_{\text{Nd}} \sim +6$  to  $+10$ ; Asahara et al., 2012; Jang et al., 2017). From 1 to 4 ka cal BP, the Nd  
362 isotopic values become more radiogenic ( $\epsilon_{\text{Nd}} \sim -4$ ), shifting towards the eastern Bering Sea

363 Water signatures ( $\epsilon_{\text{Nd}} = -2$  to  $-3$ ), as estimated from the  $\epsilon_{\text{Nd}}$  values of the Fe–Mn oxide fraction  
364 (Asahara et al., 2012). Despite the large uncertainties in the Hf isotopic composition, the overall  
365 values in core 01JPC match the overall Hf isotopic signature of the PW (Zimmermann et al.,  
366 2009a,b; Figure 3d). However, the large external uncertainties associated with the Hf isotopic  
367 values in core 01JPC do not allow the determination of Holocene changes in the PW values  
368 (Figure S2 and Table S2).

369 Overall, the  $\epsilon_{\text{Nd}}$  and  $\epsilon_{\text{Hf}}$  values from the studied sediment leachates represent the bottom  
370 seawater values in the Chukchi and Beaufort seas, and the PW (including Bering Sea and  
371 Alaskan Coastal waters), AW and Mackenzie River end members are clearly distinguishable  
372 from one another (Figure 3d and 4). The long-term Nd-Hf isotope variations observed in our bulk  
373 sediment leachates, the proportion of sediments derived from the northeastern Bering Sea and  
374 Mackenzie River (SedUnMixMC results), the amorphous silica contents and the  $\text{Log}(I+K/C+V)$   
375 ratio are discussed below in terms of changes in water sources, shelf-seawater interaction, brine  
376 formation, continental input, and possible relationships with both deglacial/Holocene climate  
377 variability and relative sea level variations.

## 378 **5.2 Role of weathering regime changes in the Nd and Hf isotopic evolution**

379 Seawater  $\epsilon_{\text{Nd}}$  and  $\epsilon_{\text{Hf}}$  values are essentially determined by the mixing of different water  
380 masses in the open ocean, whereas the interaction between dissolved and detrital fractions is  
381 significant near river mouths and continental margins (Chen et al., 2012). Several studies (Lacan  
382 & Jeandel, 2005; Pearce et al., 2013; Tachikawa et al., 1999) have discussed the exchange of  
383 material between lithogenic particles and seawater along continental margins, a process  
384 commonly referred to as boundary exchange, which is thought to play a significant role in  
385 controlling the Nd and Hf isotopic and REE compositions of the oceans. In the Arctic Ocean,

386 continental weathering plays an important role in the  $\epsilon\text{Nd}$  and  $\epsilon\text{Hf}$  values. Indeed, the authigenic  
387 Nd and Hf isotopic values of a core recovered on the Lomonosov Ridge that spans the last 14  
388 Myr were more radiogenic than those of the AW, and this difference was greater during glacial  
389 periods than during interglacial periods (Chen et al., 2012; Haley et al., 2008). These authors  
390 concluded that enhanced continental weathering together with reduced AW inflow during glacial  
391 periods was responsible for the more radiogenic values recorded on the Lomonosov Ridge. On  
392 the other hand, as described in Porcelli et al. (2009), compared to Atlantic-sourced waters, deep  
393 waters in the Canada Basin are enriched in dissolved Nd, apparently through the addition of  
394 dissolved Nd from the shelves via brine rejection. Similarly, the seawater Hf concentrations in  
395 the Canada Basin are highest at the surface and lowest in the deeper waters, suggesting the  
396 addition of river-derived Hf (notably from the Mackenzie River; Zimmermann et al., 2009a).

397 The detrital  $\epsilon\text{Nd}$  values in the northeastern Bering Sea are relatively unradiogenic ( $\sim -7$ ),  
398 suggesting that sediments are mainly derived from the Yukon River ( $\epsilon\text{Nd} \sim -8$  to  $-9$ ) and to a  
399 lesser degree from the Aleutian arc ( $\epsilon\text{Nd} \sim +6$  to  $+10$ ) (Asahara et al., 2012; Horikawa et al.,  
400 2015; Jang et al., 2017). In contrast, the detrital  $\epsilon\text{Nd}$  values in the Mackenzie area are highly  
401 unradiogenic ( $\sim -15$ ), reflecting material from the North American Craton (Maccali et al., 2018).  
402 Thus, the  $\Sigma\text{REE}$  concentrations derived from the bulk sediment leachates in cores 02PC and  
403 01JPC increase towards more unradiogenic  $\epsilon\text{Nd}$  and  $\epsilon\text{Hf}$  values between 12 and 4 ka cal BP,  
404 probably reflecting major inputs of both suspended and dissolved loads from the Mackenzie  
405 River and Yukon rivers, respectively (Figure 4b,c). We hypothesize that the major Nd and Hf  
406 inputs associated with enhanced weathering of the Mackenzie ( $\epsilon\text{Nd} \sim -12.9$ ;  $\epsilon\text{Hf} \sim -8.1$ ) and  
407 Yukon ( $\epsilon\text{Nd} \sim -8$  to  $-9$ ) river watersheds likely provided a higher contribution of unradiogenic  
408 material to cores 02PC and 01JPC during the early to mid-Holocene. Assuming that the addition  
409 of Nd and Hf by the rivers could be applied to all REEs, a period of intense weathering in the

410 Mackenzie and Yukon drainage basin may have increased the input of the dissolved  $\Sigma$ REE load  
411 and the release of material with unradiogenic Nd and Hf isotopic values into the Beaufort and  
412 Chukchi seas (Figures 3c,d and 4). Conversely, the  $\Sigma$ REE concentrations in cores 02PC and  
413 01JPC decreased during the last 4 ka cal BP, and the Hf and Nd isotopic compositions reflect  
414 more radiogenic values. These shifts are probably related to a decrease in the weathering rates in  
415 the Mackenzie and Yukon basins and enhanced inflow of PW into the Arctic Ocean (Figures 3c,d  
416 and 4).

### 417 **5.3 Causes of deglacial-Holocene seawater $\epsilon$ Nd and $\epsilon$ Hf variations**

#### 418 **5.3.1 Canadian Beaufort margin**

419 In the Canadian Beaufort margin, the Nd and Hf isotopic values from core 02PC (located  
420 at a depth of ~1000 m) exhibit a large range, from -16 to -8 for  $\epsilon$ Nd and from -10 to 5 for  $\epsilon$ Hf,  
421 implying major changes in the seawater  $\epsilon$ Nd and  $\epsilon$ Hf since the deglaciation (Figures 5h,i). Based  
422 on previous radiogenic isotope studies (Chen et al., 2012; Porcelli et al., 2009; Zimmermann et  
423 al., 2009a), we suggest that seawater  $\epsilon$ Nd and  $\epsilon$ Hf variation records in core 02PC can be  
424 interpreted mainly as the mixing of two dominant isotopic end members, namely, the Mackenzie  
425 River and AW (Figures 5h,i). The clear Mackenzie River signature recorded in core 02PC during  
426 the early Holocene ( $\epsilon$ Nd ~ -13) suggests that enhanced Mackenzie River discharge during this  
427 period induced an increase in downslope sediment transfer, resulting in a change in the bottom  
428 water Nd-Hf isotope values by particle-dissolved exchange processes (boundary exchange; Haley  
429 & Polyak, 2013; Pearce et al., 2013; Tachikawa et al., 1999). Alternatively, we cannot rule out  
430 that brine rejection resulting from sea ice formation also plays a significant role in the  
431 redistribution of dissolved Nd and Hf within the water column (Haley & Polyak, 2013).  
432 Therefore, we speculate that the higher release of dissolved and suspended loads with

433 unradiogenic Nd-Hf signatures from the Mackenzie River during the early Holocene, in  
434 conjunction with slope convection of brine-enriched shelf waters to the deeper waters,  
435 significantly influenced the bottom water Nd and Hf isotope values on the Canadian Beaufort  
436 margin. However, as there is no observational evidence for slope convection under 300 m in the  
437 Canadian Beaufort Sea (Forest et al., 2015), further investigations are needed to validate this  
438 hypothesis. In addition, the most unradiogenic Nd values ( $\epsilon_{Nd} \sim -16$ ) at approximately 11 ka cal  
439 BP coincide with the dolomite-rich IRD originating from the Canadian Arctic Archipelago  
440 (Deschamps et al., 2018a; Figure 5g,h). The geological terrain in the Canadian Arctic  
441 Archipelago are characterize by very unradiogenic Nd isotope values (-14 to -16; Maccali et al.,  
442 2018). Thus, the most unradiogenic Nd values recorded in core 02PC during the early Holocene  
443 could be explained by (1) the slight dissolution of detrital dolomite during the leaching procedure  
444 and/or (2) enhanced dolomite-rich detrital input from the Canadian Arctic Archipelago at this  
445 time (Figure 7a) and subsequent particle-dissolved exchange processes (Pearce et al., 2013).

446         Any major modification in detrital inputs from the Mackenzie River that occurred during  
447 the early to middle Holocene could not have been driven by the Laurentide Ice Sheet (LIS),  
448 which was considerably reduced in size by this time (Dyke, 2004). Wickert (2016) suggested that  
449 meltwater inputs to the Mackenzie River ended no later than 11 ka cal BP, when its eastern  
450 tributaries were temporarily rerouted eastward due to a combination of ice retreat and glacial  
451 isostatic depression. Based on permafrost studies in the Canadian Arctic (Burn, 1997; Dallimore  
452 et al., 1996), we hypothesize that the very unradiogenic  $\epsilon_{Nd}$  and  $\epsilon_{Hf}$  values recorded in core  
453 02PC during the early to middle Holocene are more likely the result of a major remobilization of  
454 readily erodible rock flour and unconsolidated sediments derived from glacially deformed terrain  
455 in the Mackenzie River watershed. The permafrost degradation in the western Canadian Arctic

456 correlates with an enhanced boreal summer insolation during the early Holocene (Figure 5a),  
457 which would have increased soil moisture storage and facilitated erosion (Burn, 1997).  
458 Furthermore, sedimentary processes in the Beaufort Sea during the early to middle Holocene  
459 were strongly influenced by regional sea level variations (Deschamps et al., 2018a; 2018b).  
460 Recently, Cornuault et al. (2018) showed that the  $\epsilon\text{Nd}$  record can be influenced by sea level  
461 variations. Similarly, the unradiogenic Nd and Hf isotopic values recorded in core 02PC showed  
462 a parallel evolution together with the relative sea level variations during the early to middle  
463 Holocene (Figure 5b). In this context, we hypothesize that low relative sea level conditions  
464 enhanced the relative influence of the Mackenzie River and Canadian Arctic Archipelago (and  
465 hence that of isotopic exchange with particles; Pearce et al., 2013) on the Canadian Beaufort  
466 Shelf during the early to middle Holocene, leading to more unradiogenic Nd and Hf isotopic  
467 values (Figures 5h,I and 7a).

468         The variability in the weathering regime on the Mackenzie River basin during the mid- to  
469 late Holocene is likely linked to changes in the precipitation patterns over the western North  
470 American continent. Indeed, previously investigations on the regional hydrologic responses to  
471 atmospheric circulation patterns during the Holocene (e.g., Barron & Anderson, 2011; Anderson  
472 et al., 2016) suggest that variations in precipitations on western North America could be  
473 controlled by changes in the large-scale atmospheric climate modes, similar to the modern El  
474 Niño Southern Oscillation (ENSO) and the Pacific Decadal Oscillation (PDO). An increased sea  
475 surface temperature in the North Pacific during a positive PDO (PDO+) phase leads to enhanced  
476 water vapor transport over the continent, thus increasing winter precipitation in western North  
477 America (Anderson et al., 2016). These conditions are reversed during a negative PDO (PDO-)  
478 phases. The transition between the mid- to late Holocene (4 ka cal BP) was characterized by a  
479 decrease in the boreal summer insolation (Figures 5a), which affected the Northern Hemisphere

480 climate system (Wanner et al., 2008). Several paleoclimate studies based on Alaskan terrestrial  
481 records (Anderson et al., 2005; Anderson et al., 2016; Barron & Anderson, 2011) and Bering  
482 Shelf marine records (Harada et al., 2014; Katsuki et al., 2009) suggest that this transition was  
483 characterized by (1) changes from a PDO+ state to a strong PDO- state (Figure 5d) and (2) a  
484 decrease in the amount of precipitation linked to a major change in the Aleutian Low intensity  
485 and position over the North Pacific. These changes are inferred to have been caused by Pacific  
486 Ocean–atmospheric dynamics attributed to an increase in El Niño frequency and a warm eastern  
487 tropical Pacific sea surface (Anderson et al., 2016; Liu et al., 2014).

488         In this context, numerical models of the regional hydrologic responses of the Mackenzie  
489 River to large-scale atmospheric circulation patterns suggest a decreasing trend in the freshwater  
490 discharges to the Canadian Beaufort margin associated with greatly reduced moisture transport  
491 over North America during the mid- to late Holocene (Figure 5e), likely driven by a reduction in  
492 the boreal summer insolation (Figure 5a) and a predominantly negative PDO-like conditions  
493 (Figure 5d; Anderson et al., 2005; 2016; Barron & Anderson, 2011; Wagner et al., 2011; Wanner  
494 et al., 2008). Thus, we suggest that this decreased discharge of the Mackenzie River also reduced  
495 the inputs of dissolved  $\Sigma$ REE and detrital material with highly unradiogenic Nd and Hf isotopic  
496 values to the Canadian Beaufort Shelf (Figure 3c). From 8 to 1 ka cal BP, the isotopic record of  
497 core 02PC increases progressively towards more radiogenic values ( $\epsilon_{Nd}$ : -9.5;  $\epsilon_{Hf}$ : 2), similar to  
498 the modern values of the AW recorded in the Canada Basin (Figures 5h and 7b,c; Porcelli et al.,  
499 2009; Zimmermann et al., 2009a). However, the  $\epsilon_{Nd}$  values observed in the Canada Basin are  
500 slightly higher than those of the water entering the North Atlantic ( $\epsilon_{Nd}$  of  $\sim$  -10.7; Porcelli et al.,  
501 2009). This difference in  $\epsilon_{Nd}$  values probably reflects the influence of the PW (Figure 7c). A  
502  $\epsilon_{Nd}$  value between -9.6 and -9.1 can be obtained by mixing 20% PW and 80% AW (Porcelli et  
503 al., 2009). Similar trends have been observed in the Nd isotopic values of a core from the Fram

504 Strait and have been attributed to PW influence (Figure 5c; Maccali et al., 2013). Thus, the  
505 changes observed in the authigenic Nd and Hf isotope signatures in core 02PC from 8 to 1 ka cal  
506 BP may likely reflect a combination of a decrease in the weathering rates within the Mackenzie  
507 River catchment and a relative increase in the influence of the AW and PW masses (Figures 5h,I  
508 and 7b,c). The enhanced PW inflows is supported by quantitative mineralogical data from the  
509 Chukchi Sea, which suggest a gradual increase in sediments delivered from the northeastern  
510 Bering Sea by the BSI after 8 ka cal BP (Deschamps et al., 2018a). Furthermore, quantitative  
511 reconstructions of past sea surface conditions (temperature, salinity, and the duration of sea ice  
512 cover), based on dinoflagellate cyst assemblages and transfer functions (Figure 5f), reveal  
513 relatively long-term stable oceanographic conditions during the late Holocene (Bringué &  
514 Rochon, 2012). However, the low resolution of our geochemical and mineralogical records  
515 prevents any linkage with the short-term variation in past sea surface conditions in the Beaufort  
516 Sea. Overall, these results suggest that the modern oceanographic conditions in the Canadian  
517 Beaufort Shelf were established during the late Holocene with the concomitant dominance of AW  
518 and PW.

### 519 **5.3.2 Chukchi-Alaskan margin**

520 In the Chukchi-Alaskan margin, our bulk sediment leachate data from core 01JPC  
521 (located at a depth of > 1000 m) show  $\epsilon\text{Nd}$  values between -6 and -4 (Figure 6e), similar to the  
522 North Pacific throughflow water signatures measured in the Bering Strait ( $\epsilon\text{Nd} \sim -6$  to  $-4$ ; Porcelli  
523 et al., 2009). Note that regional sea level variations did not influence the geochemical record in  
524 the Chukchi-Alaskan margin during the mid- to late Holocene, as these has been relatively stable  
525 during the last 6 ka cal BP (Figure 5b; Lambeck et al., 2014; Deschamps et al., 2018a). However,  
526 core 01JPC is located in an area where winter hypersaline polynya waters form through

527 additional salt input from brine rejection along the Alaska coast (Hirano et al., 2018). Based on  
528 hydrographic and satellite-derived sea ice production data obtained over the eastern Chukchi  
529 shelf and southeastern Chukchi borderland in conjunction with numerical modeling, Hirano et al.  
530 (2018) suggest that winter hypersaline polynya waters over the eastern Chukchi shelf can  
531 potentially intrude (via the Barrow Canyon) to depths comparable to or deeper than the AW layer  
532 in the Canada Basin. In this context, we hypothesize that particle-dissolved exchange processes  
533 with northeastern Bering Sea sediments and/or downflow of brine-enriched Chukchi Sea shelf  
534 waters may play a significant role in the distribution of Nd throughout the water column in the  
535 Chukchi-Alaskan margin (Haley & Polyak, 2013; Porcelli et al., 2009). These interpretations are  
536 in agreement with observations by Haley & Polyak (2013) on the surface  $\epsilon\text{Nd}$  distribution in bulk  
537 sediment leachates from the Chukchi margin. These authors speculate that modern to pre-modern  
538 distinct radiogenic  $\epsilon\text{Nd}$  signals (-6 to -4) observed on the slopes of the Chukchi margin and  
539 adjacent borderland could be indicative of PW convection (e.g., via brine rejection) and/or  
540 persistent sediment redistribution from the Chukchi shelf. Overall, although we acknowledge that  
541 direct observations are needed to validate the deep-water convection driven by brines in the  
542 Chukchi-Alaskan margin, our results support the hypothesis that both boundary exchange and  
543 brine rejection during sea ice formation have probably influenced the distribution of radiogenic  
544 isotope (such as Nd and Hf) compositions in western Arctic seawater for the last 6 ka cal BP.

545         The authigenic  $\epsilon\text{Nd}$  record obtained in core 01JPC allows a close look at the changes in  
546 the relative contributions between the two main components of the BIS (Figures 6e and 7b,c): (1)  
547 Alaskan Coastal Water characterized by more unradiogenic Nd isotope compositions ( $\epsilon\text{Nd} \sim -8$  to  
548  $-9$ ), which reflect the dissolved Nd inputs from the Yukon drainage basin (e.g., VanLaningham et  
549 al., 2009; Horikawa et al., 2010, 2015), and (2) Bering Sea Water, which has more radiogenic Nd  
550 isotope compositions ( $\epsilon\text{Nd} \sim -2$  to  $-3$ ) mainly derived from the western Bering Sea (i.e., coastal

551 water adjacent to the Anadyr region and Bering Shelf; Asahara et al., 2012; Jang et al., 2017).  
552 Thus, the more radiogenic  $\epsilon\text{Nd}$  values ( $\sim -2$ ) found on the Chukchi shelf can be explained by a  
553 high contribution of Bering Sea Water to the BSI and/or less influence of the Yukon River  
554 discharge to the Alaskan Coastal waters (Figure 7c). In this context, and as previously discussed,  
555 large-scale atmospheric climate modes, such as the PDO, provide a potential mechanistic  
556 explanation for correlations between changes in the precipitation patterns over North America  
557 and the position of the Aleutian Low in the North Pacific, as well as explaining changes in the  
558 BSI (Anderson et al., 2016; Yamamoto et al., 2017). The winter precipitation patterns result from  
559 the strength and position of the Aleutian Low, which is strengthened and/or located farther to the  
560 east of the North Pacific during a PDO+ phase and weakened and/or located more to the west of  
561 the North Pacific during a PDO- phase (Barron & Anderson, 2011). In addition, modern data  
562 from the Yukon River suggest a positive trend in the annual flow during PDO+ phases, perhaps  
563 reflecting the increases in annual precipitation in the interior of Alaska (Brabets and Walvoord,  
564 2009).

565         Within this context, we hypothesize that the wetter conditions associated with the PDO+  
566 state in conjunction with an enhanced boreal summer insolation during the middle Holocene  
567 (Figure 6a,b; Anderson et al., 2016; Liu et al., 2014) may have promoted higher weathering rates  
568 in the Yukon drainage basin, which is consistent with the high unradiogenic  $\epsilon\text{Nd}$  values recorded  
569 in core 01JPC (Figures 6e and 7b). Conversely, during the late Holocene, the drier negative PDO-  
570 like conditions in western North America (Figure 6b), together with an long-term decrease in  
571 boreal summer insolation (Figure 6a), likely reduced the weathering rates in the Yukon drainage  
572 basin and therefore produced a relative increase in the contribution of dissolved and detrital loads  
573 with more radiogenic values from the Bering Sea Water to the BSI (Figure 7c). Likewise, the  
574 decrease in the  $\text{Log}(I+K/C+V)$  ratio and the relative increase in the proportions of the

575 northeastern Bering Sea sediments (SedUnMixMC results) and amorphous silica (proxy for the  
576 BSI intensity; Jakobsson et al., 2017; Stein et al., 2017) in core 01JPC are also in agreement with  
577 increases in the BSI during the late Holocene (Figure 6f-h).

578         The strength and distribution of BSI water between different branches (Figure 7b,c)  
579 influences the sea surface temperatures and the spatial and temporal variability of the sea ice  
580 cover in the Chukchi Sea (e.g., Shimada et al., 2006; McKay et al., 2008; Polyak et al., 2016;  
581 Stein et al., 2017). For example, the results from transfer functions based on dinoflagellate cyst  
582 assemblages from the nearby core 05JPC (McKay et al., 2008) suggest a decrease in the duration  
583 of sea ice cover and an increase in summer sea surface temperatures after 4 ka cal BP relative to  
584 the middle Holocene (between 6 and 4 ka cal BP) in the northeastern Chukchi Sea (Figure 6d). In  
585 contrast, based on sea ice biomarker proxy records from two sediment cores from the  
586 northwestern Chukchi Sea (ARA2B-1A) and East Siberian Sea (PS72/350-2), Stein et al. (2017)  
587 suggested a significantly increased sea ice extent during the last 4.5 ka cal BP relative to the  
588 middle Holocene (Figure 6c). These differences in the sea ice extent in the Chukchi Sea seem to  
589 be related to changes in the circulation of the BSI across the Chukchi shelf (Figure 7b,c), which is  
590 itself modulated by changes in the PDO phase (e.g., Screen and Francis, 2016). Based on  
591 numerical models, Winsor and Chapman (2004) suggest that predominantly northeasterly to  
592 easterly winds in the northernmost Pacific, usually dominant during PDO+ phases (Zhang et al.,  
593 2015), produce an overall reduction in the BSI (induced by an enhanced Aleutian Low) and  
594 induce a more northwestward direction to the BSI across the Chukchi shelf edge (Figure 7b).  
595 These PDO-like ocean-atmosphere conditions were likely responsible for the sea ice reduction  
596 observed in the northwestern Chukchi Sea and East Siberian Sea during the middle Holocene  
597 (Stein et al., 2017). Conversely, sustained westerly winds from the northernmost Pacific, usually  
598 dominant during PDO- (Zhang et al., 2015), produce an overall intensified BSI (induced by a

599 weakened Aleutian Low) and favor north-northeast diversion of the BSI through the Central  
600 Channel and along the Chukchi-Alaskan coast (Figure 7c; Winsor and Chapman, 2004). These  
601 atmospheric and oceanographic conditions probably promoted reduced sea ice cover and an  
602 increase in sea surface temperatures in the northeastern Chukchi Sea during the last 4 ka cal BP  
603 (McKay et al., 2008). Overall, this spatial and temporal variability in the sea ice cover in the  
604 Chukchi Sea (Figure 6c,d) supports our interpretation of not only an increase in the relative  
605 proportion of the Bering Sea Water component of the BSI (Figures 6e-h) but also major  
606 northeastward diversion of the BSI in the Chukchi Sea during the late Holocene (Figure 7c).

607         Although we recognize that the links with PDO-like ocean-atmosphere interactions  
608 warrant further study, evidence of enhanced PDO expression along the northeastern Pacific  
609 margins during the late Holocene relative to the middle Holocene (Figure 6b; Barron &  
610 Anderson, 2011) is a sufficient explanation of the long-term variability that we observe in our  
611 paleoceanographic records. A study with a higher temporal (e.g., centennial to millennial scale)  
612 resolution that couples quantitative mineralogy and radiogenic isotope data during this period  
613 needs to be performed to provide a better understanding of the relationships among the  
614 atmospheric climate mode (e.g., PDO), continental weathering and the BSI.

## 615 **6 Conclusion**

616         Using the combined Nd and Hf isotopic record from bulk sediment leachates in two piston  
617 cores recovered from the Canadian Beaufort (02PC) and Chukchi-Alaskan (01JPC) margins, we  
618 investigated changes in weathering regimes and deep-water circulation during the Holocene.  
619 Overall, our mineralogical and Nd-Hf isotopic data, together with modeled Holocene Arctic river  
620 discharges (Wagner et al., 2011), quantitative reconstructions of past sea surface conditions

621 (McKay et al., 2008; Stein et al., 2017), and hypothesized changes in atmospheric circulation  
622 (Winsor and Chapman, 2004; Barron & Anderson, 2011), reveal the following:

623 (1) A clear Mackenzie River and PW isotopic signature at coring sites 02PC and 01JPC at  
624 approximately 1000 m supports the hypothesis that brine rejection during sea ice formation  
625 and/or persistent sediment redistribution from the shelf probably plays significant roles in  
626 controlling the  $\epsilon\text{Nd}$  and  $\epsilon\text{Hf}$  values of the bottom waters of the Canadian Beaufort and Chukchi-  
627 Alaskan margins.

628 (2) Since the last deglacial period, the Nd and Hf isotopic compositions of bulk sediment  
629 leachates from the Beaufort Sea core transition from resembling those of the Mackenzie River  
630 end member to resembling those of the AW end member. The Mackenzie River-like values are  
631 linked to the remobilization of rock flour from glacially deformed terrain in the Mackenzie River  
632 watershed and lower sea level conditions during the early Holocene. In the middle to late  
633 Holocene, the shift towards AW-like isotopic values is inferred to be the result of a decrease in  
634 the Mackenzie River discharge, likely associated with predominantly negative PDO-like  
635 conditions.

636 (3) The Nd and Hf isotopic compositions of bulk sediment leachates in the Chukchi-Alaskan  
637 margin were controlled by (1) more intense precipitation and weathering in the drainage basin of  
638 the Yukon River during the middle Holocene and (2) drier conditions and an increase in the  
639 relative contribution of the Bering Sea Water component to the BSI during the late Holocene.  
640 This transition seems to have resulted from major changes in atmospheric climate modes induced  
641 by a PDO/ENSO-like forcing.

642

643 **Acknowledgments**

644 We sincerely thank the captains, officers, crew and scientists on board the USCGC Healy  
645 and the CCGS Amundsen for the recovery the cores used in this study. These cores were  
646 collected as part of the HOTRAX expedition (USCGC Healy), as well as the CASES and  
647 ArcticNet (CCGS Amundsen) programs. We also thank Quentin Beauvais (UQAR-ISMER),  
648 Mathieu Babin (UQAR-ISMER), and Adriana Gamboa (UQAR-ISMER and UDO) for their  
649 technical support and advice in the laboratory. This research was funded ArcticNet and by the  
650 Natural Sciences and Engineering Research Council of Canada (NSERC) through Discovery  
651 Grants to J.-C. Montero-Serrano and G. St-Onge, as well as through ship time support for several  
652 expeditions (J.-C. Montero-Serrano and G. St-Onge). Finally, thanks to: Thomas Barbour and  
653 American Journal Experts for reviewing the grammar; the two anonymous reviewers for their  
654 constructive review which improve the quality of the manuscript; and Ellen Thomas and  
655 Christopher Reinhard for their editorial work. All analytical data presented are available  
656 electronically in the Supplementary Appendix (Tables S1 and S5) and PANGAEA database at  
657 <https://doi.pangaea.de/10.1594/PANGAEA.897880>.

## 658 **7 References**

- 659 Abbott, A. N., Haley, B. A., and McManus, J. (2016). The impact of sedimentary coatings on the  
660 diagenetic Nd flux. *Earth Planet. Sci. Lett.* 449, 217–227. doi:  
661 10.1016/j.epsl.2016.06.001.
- 662 Albarède, F., Simonetti, A., Vervoort, J. D., Blichert-Toft, J. & Abouchami, W. (1998). A Hf-Nd  
663 isotopic correlation in ferromanganese nodules. *Geophysical Research Letters*, 25, 3895-  
664 3898. <https://doi.org/10.1029/1998GL900008>.
- 665 Anderson, L., Abbott, M. B., Finney, B. P. & Burns, S. J. (2005). Regional atmospheric  
666 circulation change in the North Pacific during the Holocene inferred from lacustrine  
667 carbonate oxygen isotopes, Yukon Territory, Canada. *Quaternary Research*, 64, 21-35.  
668 <https://doi.org/10.1016/j.yqres.2005.03.005>.
- 669 Anderson, L., Berkelhammer, M., Barron, J. A., Steinman, B. A., Finney, B. P. & Abbott, M. B.  
670 (2016). Lake oxygen isotopes as recorders of North American Rocky Mountain  
671 hydroclimate: Holocene patterns and variability at multi-decadal to millennial time scales.  
672 *Global and Planetary Change*, 137, 131-148.  
673 <https://doi.org/10.1016/j.gloplacha.2015.12.021>.

- 674 Andrews, J. T. & Dunhill, G. (2004). Early to mid-Holocene Atlantic water influx and deglacial  
675 meltwater events, Beaufort Sea slope, Arctic Ocean. *Quaternary Research*, 61, 14-21.  
676 <https://doi.org/10.1016/j.yqres.2003.08.003>.
- 677 Andrews, J. T. & Eberl, D. D. (2012). Determination of sediment provenance by unmixing the  
678 mineralogy of source-area sediments: The “SedUnMix” program. *Marine Geology*, 291-  
679 294, 24-33. <https://doi.org/10.1016/j.margeo.2011.10.007>.
- 680 Andrews, J. T., Stein, R., Moros, M. & Perner, K. (2016). Late Quaternary changes in sediment  
681 composition on the NE Greenland margin (~73° N) with a focus on the fjords and shelf.  
682 *Boreas*, 45, 381-397.
- 683 Asahara, Y., Takeuchi, F., Nagashima, K., Harada, N., Yamamoto, K., Oguri, K. & Tadai, O.  
684 (2012). Provenance of terrigenous detritus of the surface sediments in the Bering and  
685 Chukchi Seas as derived from Sr and Nd isotopes: Implications for recent climate change  
686 in the Arctic regions. *Deep-Sea Research Part II: Topical Studies in Oceanography*, 61-  
687 64, 155-171. <https://doi.org/10.1016/j.dsr2.2011.12.004>.
- 688 Barron, J. A. & Anderson, L. (2011). Enhanced Late Holocene ENSO/PDO expression along the  
689 margins of the eastern North Pacific. *Quaternary International*, 235, 3-12.  
690 <https://doi.org/10.1016/j.quaint.2010.02.026>.
- 691 Bayon, G., German, C. R., Burton, K. W., Nesbitt, R. W. & Rogers, N. (2004). Sedimentary Fe-  
692 Mn oxyhydroxides as paleoceanographic archives and the role of aeolian flux in  
693 regulating oceanic dissolved REE. *Earth and Planetary Science Letters*, 224, 477-492.  
694 <https://doi.org/10.1016/j.epsl.2004.05.033>.
- 695 Berger, A. & Loutre, M. F. (1991). Insolation values for the climate of the last 10 million years.  
696 *Quaternary Science Reviews*, 10, 297-317. [https://doi.org/10.1016/0277-3791\(91\)90033-  
697 Q](https://doi.org/10.1016/0277-3791(91)90033-Q).
- 698 Birck, J. L. (1986). Precision K-Rb-Sr isotopic analysis: Application to Rb-Sr chronology.  
699 *Chemical Geology*, 56, 73-83. [https://doi.org/10.1016/0009-2541\(86\)90111-7](https://doi.org/10.1016/0009-2541(86)90111-7).
- 700 Biscaye, P. E. (1965). Mineralogy and Sedimentation of Recent Deep-Sea Clay in the Atlantic  
701 Ocean and Adjacent Seas and Oceans. *Geological Society of America Bulletin*, 76, 803-  
702 832. [https://doi.org/10.1130/0016-7606\(1965\)76\[803:MASORD\]2.0.CO;2](https://doi.org/10.1130/0016-7606(1965)76[803:MASORD]2.0.CO;2).
- 703 Bout-Roumazeilles, V., Cortijo, E., Labeyrie, L. & Debrabant, P. (1999). Clay mineral evidence  
704 of nepheloid layer contributions to the Heinrich layers in the northwest Atlantic.  
705 *Palaeogeography, Palaeoclimatology, Palaeoecology*, 146, 211-228.  
706 [https://doi.org/10.1016/S0031-0182\(98\)00137-0](https://doi.org/10.1016/S0031-0182(98)00137-0).
- 707 Burn, C. R. (1997). Cryostratigraphy, paleogeography, and climate change during the early  
708 Holocene warm interval, western Arctic coast, Canada. *Canada Journal of Earth Science*,  
709 34, 912-925. <https://doi.org/10.1139/e17-076>.
- 710 Chen, T. Y., Frank, M., Haley, B. a., Gutjahr, M. & Spielhagen, R. F. (2012). Variations of North  
711 Atlantic inflow to the central Arctic Ocean over the last 14 million years inferred from  
712 hafnium and neodymium isotopes. *Earth and Planetary Science Letters*, 353-354, 82-92.  
713 <https://doi.org/10.1016/j.epsl.2012.08.012>.
- 714 Corlett, W. B. & Pickart, R. S. (2017). The Chukchi slope current. *Progress in Oceanography*,  
715 153, 50-65. <https://doi.org/10.1016/j.pocean.2017.04.005>.
- 716 Cornuault, M., Tachikawa, K., Vidal, L., Guihou, A., Siani, G., Deschamps, P., Bassinot, F. &  
717 Revel, M. (2018). Circulation Changes in the Eastern Mediterranean Sea Over the Past  
718 23,000 Years Inferred From Authigenic Nd Isotopic Ratios. *Paleoceanography and  
719 Paleoclimatology*. <https://doi.org/10.1002/2017PA003227>.

- 720 Dallimore, S. R., Wolfe, S. A. & Solomon, S. M. (1996). Influence of ground ice and permafrost  
721 on coastal evolution, Richards Island, Beaufort Sea coast, N.W.T. *Canadian Journal of*  
722 *Earth Sciences*, 33, 664-675. <https://doi.org/10.1139/e96-050>.
- 723 Danielson, S. L., Weingartner, T. J., Hedstrom, K. S., Aagaard, K., Woodgate, R., Curchitser, E.  
724 & Stabeno, P. J. (2014). Coupled wind-forced controls of the Bering–Chukchi shelf  
725 circulation and the Bering Strait throughflow: Ekman transport, continental shelf waves,  
726 and variations of the Pacific–Arctic sea surface height gradient. *Progress in*  
727 *Oceanography*, 125, 40-61. <https://doi.org/10.1016/j.pocean.2014.04.006>.
- 728 Darby & Bischof (2004). A Holocene record of changing Arctic Ocean ice drift analogous to the  
729 effects of the Arctic Oscillation. *Paleoceanography*, 19, 1-9.
- 730 Darby, D. A., Myers, W. B., Jakobsson, M. & Rigor, I. (2011). Modern dirty sea ice  
731 characteristics and sources: The role of anchor ice. *Journal of Geophysical Research:*  
732 *Oceans*, 116, 1-18. <https://doi.org/10.1029/2003PA000961>.
- 733 Darby, D. A., Ortiz, J., Polyak, L., Lund, S., Jakobsson, M. & Woodgate, R. A. (2009). The role  
734 of currents and sea ice in both slowly deposited central Arctic and rapidly deposited  
735 Chukchi-Alaskan margin sediments. *Global and Planetary Change*, 68, 58-72.  
736 <https://doi.org/10.1016/j.gloplacha.2009.02.007>.
- 737 Darby, D. A. & Zimmerman, P. (2008). Ice-rafted detritus events in the Arctic during the last  
738 glacial interval, and the timing of the Innuitian and Laurentide ice sheet calving events.  
739 *Polar Research*, 27, 114-127. <https://doi.org/10.1111/j.1751-8369.2008.00057.x>.
- 740 Deschamps, C.-E., Montero-serrano, J.-C. & St-Onge, G. (2018a). Sediment provenance changes  
741 in the western Arctic Ocean in response to ice-rafting, sea-level and oceanic circulation  
742 variations since the last deglaciation. *Geochemistry Geophysics Geosystems*.  
743 <https://doi.org/10.1029/2017GC007411>.
- 744 Deschamps, C.-E., St-Onge, G., Montero-Serrano, J.-C. & Polyak, L. (2018b).  
745 Chronostratigraphy and spatial distribution of the Chukchi and Beaufort Sea's magnetic  
746 sediments since the last deglaciation. *Boreas*, 47, 544-564.  
747 <https://doi.org/10.1111/bor.12296>.
- 748 Deschamps, C. E. 2018: Dynamique sédimentaire et paléocéanographique le long des  
749 marges continentales des mers de Beaufort et des Tchouktches (océan Arctique) depuis la  
750 dernière déglaciation. (Doctoral dissertation). UQAR-ISMER, Rimouski.
- 751 Dickson, R., Rudels, B., Dye, S., Karcher, M., Meincke, J. & Yashayaev, I. (2007). Current  
752 estimates of freshwater flux through Arctic and subarctic seas. *Progress in*  
753 *Oceanography*, 73, 210-230. <https://doi.org/10.1016/j.pocean.2006.12.003>.
- 754 Du, J., Haley, B. A. & Mix, A. C. (2016). Neodymium isotopes in authigenic phases, bottom  
755 waters and detrital sediments in the Gulf of Alaska and their implications for paleo-  
756 circulation reconstruction. *Geochimica et Cosmochimica Acta*, 193, 14-35.  
757 <https://doi.org/10.1016/j.gca.2016.08.005>.
- 758 Dyke, A. S. (2004). An outline of the deglaciation of North America with emphasis on central  
759 and northern Canada. *Quaternary Glaciations-Extent and Chronology, Part II: North*  
760 *America, 2b*, 373-424. [https://doi.org/10.1016/S1571-0866\(04\)80209-4](https://doi.org/10.1016/S1571-0866(04)80209-4).
- 761 Eberl, D. D. (2003). User guide to RockJock—A program for determining quantitative  
762 mineralogy from X-ray diffraction data. *USGS Open File Report, OF 03-78*, 40.
- 763 Forest, A., Osborne, P. D., Fortier, L., Sampei, M. & Lowings, M. G. (2015). Physical forcings  
764 and intense shelf – slope fluxes of particulate matter in the halocline waters of the  
765 Canadian Beaufort Sea during winter. *Continental Shelf Research*, 101, 1-21.  
766 <https://doi.org/10.1016/j.csr.2015.03.009>.

767 Forest, A., Tremblay, J. É., Gratton, Y., Martin, J., Gagnon, J., Darnis, G., Sampei, M., Fortier,  
768 L., Ardyna, M., Gosselin, M., Hattori, H., Nguyen, D., Maranger, R., Vaqué, D., Marrasé,  
769 C., Pedrós-Alió, C., Sallon, A., Michel, C., Kellogg, C., Deming, J., Shadwick, E.,  
770 Thomas, H., Link, H., Archambault, P. & Piepenburg, D. (2011). Biogenic carbon flows  
771 through the planktonic food web of the Amundsen Gulf (Arctic Ocean): A synthesis of  
772 field measurements and inverse modeling analyses. *Progress in Oceanography*, 91, 410-  
773 436. <https://doi.org/10.1016/j.pocean.2011.05.002>.

774 Frank, M. (2002). Radiogenic isotopes: Tracers of past ocean circulation and erosional input.  
775 *Reviews of Geophysics*, 40. <https://doi.org/10.1029/2000RG000094>.

776 Funk, J. A., 2004. Sediment Accumulation and Diagenesis in the Late Quaternary Equatorial  
777 Atlantic Ocean : An Environmental Magnetic and Geochemical Perspective. Ph.D. thesis,  
778 Universitat Bremen. 103 p.

779 Gamboa, A., Montero-Serrano, J.-C., St-Onge, G., Rochon, A. & Desiège, P.-A. (2017).  
780 Mineralogical, geochemical and magnetic signatures of surface sediments from the  
781 Canadian Beaufort Shelf and Amundsen Gulf (Canadian Arctic). *Geochemistry,*  
782 *Geophysics, Geosystems*, 18, 488-512. <https://doi.org/10.1002/2016GC006477>.

783 Grebmeier, J.M., Cooper, L.W., Feder, H.M., Sirenko, B.I. (2006). Ecosystem dynamics of the  
784 Pacific-influenced northern Bering and Chukchi Seas in the Amerasian Arctic. *Progress in*  
785 *Oceanography* 71: 331–361

786 Gutjahr, M., Frank, M., Lippold, J. & Halliday, A. N. (2014). Peak Last Glacial weathering  
787 intensity on the North American continent recorded by the authigenic Hf isotope  
788 composition of North Atlantic deep-sea sediments. *Quaternary Science Reviews*, 99, 97-  
789 111. <https://doi.org/10.1016/j.quascirev.2014.06.022>.

790 Gutjahr, M., Frank, M., Stirling, C. H., Klemm, V., van de Flieddt, T. & Halliday, A. N. (2007).  
791 Reliable extraction of a deepwater trace metal isotope signal from Fe-Mn oxyhydroxide  
792 coatings of marine sediments. *Chemical Geology*, 242, 351-370.  
793 <https://doi.org/10.1016/j.chemgeo.2007.03.021>.

794 Gutjahr, M., Hoogakker, B. a. a., Frank, M. & McCave, I. N. (2010). Changes in North Atlantic  
795 Deep Water strength and bottom water masses during Marine Isotope Stage 3 (45-  
796 35kaBP). *Quaternary Science Reviews*, 29, 2451-2461.  
797 <https://doi.org/10.1016/j.quascirev.2010.02.024>.

798 Haley, B. A., Frank, M., Spielhagen, R. F. & Fietzke, J. (2008). Radiogenic isotope record of  
799 Arctic Ocean circulation and weathering inputs of the past 15 million years.  
800 *Paleoceanography*, 23. <https://doi.org/10.1029/2007PA001486>.

801 Haley, B. A., Klinkhammer, G. P. & McManus, J. (2004). Rare earth elements in pore waters of  
802 marine sediments. *Geochimica et Cosmochimica Acta*, 68, 1265-1279.  
803 <https://doi.org/10.1016/j.gca.2003.09.012>.

804 Haley, B. A. & Polyak, L. (2013). Pre-modern Arctic Ocean circulation from surface sediment  
805 neodymium isotopes. *Geophysical Research Letters*, 40, 893-897.  
806 <https://doi.org/10.1002/grl.50188>.

807 Haley, B.A., Du, J., Abbott, A.N. & McManus, J. (2017). The Impact of Benthic Processes on  
808 Rare Earth Element and Neodymium Isotope Distributions in the Oceans. *Front. Mar. Sci.*  
809 4:426. doi: 10.3389/fmars.2017.00426

810 Harada, N., Katsuki, K., Nakagawa, M., Matsumoto, A., Seki, O., Addison, J. A., Finney, B. P. &  
811 Sato, M. (2014). Holocene sea surface temperature and sea ice extent in the Okhotsk and  
812 Bering Seas. *Biogeochemical and physical processes in the Sea of Okhotsk and the*

813 *linkages to the Pacific Ocean*, 126, 242-253.  
814 <https://doi.org/10.1016/j.pocean.2014.04.017>.

815 Hill, J. C. & Driscoll, N. W. (2008). Paleodrainage on the Chukchi shelf reveals sea level history  
816 and meltwater discharge. *Marine Geology*, 254, 129-151.  
817 <https://doi.org/10.1016/j.margeo.2008.05.018>.

818 Hirano, D., Fukamachi, Y., Ohshima, K. I., Watanabe, E., Mahoney, A. R., Eicken, H., Itoh, M.,  
819 Simizu, D., Iwamoto, K., Jones, J., Takatsuka, T., Kikuchi, T., Tamura, T. (2018). Winter  
820 water formation in coastal polynyas of the eastern Chukchi shelf: Pacific and Atlantic  
821 influences. *Journal of Geophysical Research: Oceans*, 123, 5688–5705.  
822 <https://doi.org/10.1029/2017JC013307>.

823 Hofmann, D. I., Fabian, K. (2009). Correcting relative paleointensity records for variations in  
824 sediment composition: Results from a South Atlantic stratigraphic network. *Earth and*  
825 *Planetary Science Letters* 284 (1-2), 34-43.

826 Hofmann, D. I., Fabian, K., Schmieder, F., Donner, B., Bleil, U. (2005). A stratigraphic network  
827 across the Subtropical Front in the central South Atlantic: Multi-parameter correlation of  
828 magnetic susceptibility, density, X-ray fluorescence and <sup>18</sup>O records. *Earth and Planetary*  
829 *Science Letters* 240 (3-4), 694-709.

830 Horikawa, K., Martin, E.E., Basak, C., Onodera, J., Seki, O., Sakamoto, T., Ikehara, M., Sakai,  
831 S., Kawamura, K. (2015). Pliocene cooling enhanced by flow of low-salinity Bering Sea  
832 water to the Arctic Ocean. *Nat. Commun.* 6, 7587, doi: 10.1038/ncomms8587.

833 Horikawa, K., Asahara, Y., Yamamoto, K. & Okazaki, Y. (2010). Intermediate water formation  
834 in the Bering Sea during glacial periods: Evidence from neodymium isotope ratios.  
835 *Geology*, 38, 435-438. <https://doi.org/10.1130/G30225.1>.

836 Jacobsen, S. B. & Wasserburg, G. J. (1980). Sm-Nd isotopic evolution of chondrites. *Earth and*  
837 *Planetary Science Letters*, 50, 139-155. [https://doi.org/10.1016/0012-821X\(80\)90125-9](https://doi.org/10.1016/0012-821X(80)90125-9).

838 Jang, K., Huh, Y., Han, Y. (2017). Authigenic Nd isotope record of North Pacific Intermediate  
839 Water formation and boundary exchange on the Bering Slope. *Quat. Sci. Rev.* 156, 150–  
840 163.

841 Jakobsson, M., Pearce, C., Cronin, T. M., Backman, J., Anderson, L. G., Barrientos, N., Björk,  
842 G., Coxall, H., de Boer, A., Mayer, L. A., Mörth, C.-M., Nilsson, J., Rattray, J. E.,  
843 Stranne, C., Semilietov, I., amp, apos & Regan, M. (2017). Post-glacial flooding of the  
844 Beringia Land Bridge dated to 11 cal ka BP based on new geophysical and sediment  
845 records. *Climate of the Past Discussions*, 13, 991-1005. [https://doi.org/10.5194/cp-13-](https://doi.org/10.5194/cp-13-991-2017)  
846 991-2017

847 Jeandel, C., Arsouze, T., Lacan, F., Téchiné, P. & Dutay, J. C. (2007). Isotopic Nd compositions  
848 and concentrations of the lithogenic inputs into the ocean: A compilation, with an  
849 emphasis on the margins. *Chemical Geology*, 239, 156-164.  
850 <https://doi.org/10.1016/j.chemgeo.2006.11.013>.

851 Katsuki, K., Khim, B. K., Itaki, T., Harada, N., Sakai, H., Ikeda, T., Takahashi, K., Okazaki, Y.  
852 & Asahi, H. (2009). Land-sea linkage of Holocene paleoclimate on the southern bering  
853 continental shelf. *Holocene*, 19, 747-756. <https://doi.org/10.1177/0959683609105298>.

854 Kinnard, C., Zdanowicz, C. M., Fisher, D. A., Isaksson, E., de Vernal, A. & Thompson, L. G.  
855 (2011). Reconstructed changes in Arctic sea ice over the past 1,450 years. *Nature*, 479,  
856 509-512. <https://doi.org/10.1038/nature10581>.

857 Kobayashi, D., Yamamoto, M., Irino, T., Nam, S.-I., Park, Y.-H., Harada, N., Nagashima, K.,  
858 Chikita, K. & Saitoh, S.-I. (2016). Distribution of detrital minerals and sediment color in  
859 western Arctic Ocean and northern Bering Sea sediments: Changes in the provenance of

860 western Arctic Ocean sediments since the last glacial period. *Polar Science*, 10, 519-531.  
861 <https://doi.org/10.1016/j.polar.2016.07.005>.

862 Lacan, F. & Jeandel, C. (2005). Neodymium isotopes as a new tool for quantifying exchange  
863 fluxes at the continent-ocean interface. *Earth and Planetary Science Letters*, 232, 245-  
864 257. <https://doi.org/10.1016/j.epsl.2005.01.004>.

865 Lambeck, K., Rouby, H., Purcell, A., Sun, Y. & Sambridge, M. (2014). Sea level and global ice  
866 volumes from the Last Glacial Maximum to the Holocene. *Proceedings of the National  
867 Academy of Sciences*, 111, 15296-15303. <https://doi.org/10.1073/pnas.1411762111>.

868 Li, C.-F., Guo, J.-H., Yang, Y.-H., Chu, Z.-Y. & Wang, X.-C. (2014). Single-step separation  
869 scheme and high-precision isotopic ratios analysis of Sr–Nd–Hf in silicate materials. *J.  
870 Anal. At. Spectrom.*, 29, 1467-1476. <https://doi.org/10.1039/C3JA50384D>

871 Liu, Z., Yoshimura, K., Bowen, G. J., Buening, N. H., Risi, C., Welker, J. M. & Yuan, F.  
872 (2014). Paired oxygen isotope records reveal modern North American atmospheric  
873 dynamics during the Holocene. *Nature Communications*, 5, 1-7.  
874 <https://doi.org/10.1038/ncomms4701>.

875 Maccali, J., Hillaire-Marcel, C., Carignan, J. & Reisberg, L. C. (2013). Geochemical signatures  
876 of sediments documenting Arctic sea-ice and water mass export through Fram Strait since  
877 the Last Glacial Maximum. *Quaternary Science Reviews*, 64, 136-151.  
878 <https://doi.org/10.1016/j.quascirev.2012.10.029>.

879 Maccali, J., Hillaire-Marcel, C. & Not, C. (2018). Radiogenic isotope (Nd, Pb, Sr) signatures of  
880 surface and sea ice-transported sediments from the Arctic Ocean under the present  
881 interglacial conditions. *Polar Research*, 37, 1442982.  
882 <https://doi.org/10.1080/17518369.2018.1442982>.

883 Macdonald R. W. and Gobeil C. (2012). Manganese Sources and Sinks in the Arctic Ocean with  
884 Reference to Periodic Enrichments in Basin Sediments. *Aquat. Geochem.* 18, 565-591.

885 McKay, J. L., de Vernal, A., Hillaire-Marcel, C., Not, C., Polyak, L. & Darby, D. (2008).  
886 Holocene fluctuations in Arctic sea-ice cover: dinocyst-based reconstructions for the  
887 eastern Chukchi Sea. *Canadian Journal of Earth Sciences*, 45, 1377-1397.  
888 <https://doi.org/10.1139/E08-046>.

889 McManus, J. F., Francois, R., Gherardi, J. M., Keigwin, L. D. & Brown-Leger, S. (2004).  
890 Collapse and rapid resumption of Atlantic meridional circulation linked to deglacial  
891 climate changes. *Nature*, 428, 834-837. <https://doi.org/10.1038/nature02494>.

892 Meinhardt, A.-K., März, C., Schuth, S., Lettmann, K.A., Schnetger, B., Wolff, J.-O., Brumsack,  
893 H.-J. (2016b) Diagenetic regimes in Arctic Ocean sediments: Implications for sediment  
894 geochemistry and core correlation. *Geochimica et Cosmochimica Acta* 188, 125-146.

895 Meinhardt, A. K., Pahnke, K., Böning, P., Schnetger, B. & Brumsack, H. J. (2016a). Climate  
896 change and response in bottom water circulation and sediment provenance in the Central  
897 Arctic Ocean since the Last Glacial. *Chemical Geology*, 427, 98-108.  
898 <https://doi.org/10.1016/j.chemgeo.2016.02.019>.

899 Molina-Kescher, M., Frank, M. & Hathorne, E. C. (2014). Nd and Sr isotope compositions of  
900 different phases of surface sediments in the South Pacific: Extraction of seawater  
901 signatures, boundary exchange, and detrital/dust provenance. *Geochemistry, Geophysics,  
902 Geosystems*, 15, 3502-3520. <https://doi.org/10.1002/2014GC005443>.

903 Nelson, H., Creager, J.S. (1977). Displacement of Yukon-derived sediment from the Bering Sea  
904 to the Chukchi Sea during Holocene time. *Geology* 5, 141–146.

905 Nowell, G. M., Kempton, P. D., Noble, S. R., Saunders, a. D., Mahoney, J. J. & Taylor, R. N.  
906 (1998). High-precision Hf isotopic measurements of MORB and OIB by thermal

907 ionization mass-spectrometry: insights into the depleted mantle. *Chemical Geology*, 149,  
908 211-233. [https://doi.org/10.1016/S0009-2541\(98\)00036-9](https://doi.org/10.1016/S0009-2541(98)00036-9).

909 Okkonen, S. R., Ashjian, C. J., Campbell, R. G., Maslowski, W., Clement-Kinney, J. L. & Potter,  
910 R. (2009). Intrusion of warm Bering/Chukchi waters onto the shelf in the western  
911 Beaufort Sea. *Journal of Geophysical Research*, 114, 1-23.  
912 <https://doi.org/10.1029/2008JC004870>.

913 Osborne, P.D. and Forest, A. (2016). Sediment dynamics from coast to slope – Southern  
914 Canadian Beaufort Sea. In: Vila-Concejo, A.; Bruce, E.; Kennedy, D.M., and McCarroll,  
915 R.J. (eds.), Proceedings of the 14th International Coastal Symposium (Sydney, Australia).  
916 *Journal of Coastal Research*, Special Issue, No. 75, 537-541.

917 Pearce, C. R., Jones, M. T., Oelkers, E. H., Pradoux, C. & Jeandel, C. (2013). The effect of  
918 particulate dissolution on the neodymium (Nd) isotope and Rare Earth Element (REE)  
919 composition of seawater. *Earth and Planetary Science Letters*, 369-370, 138-147.  
920 <https://doi.org/10.1016/j.epsl.2013.03.023>.

921 Petschick, R. (2000). MacDiff 4.2. 5 Manual. *Institut für Geologie, Universität Erlangen:*  
922 *Germany*.

923 Pickart, R. S. (2004). Shelfbreak circulation in the Alaskan Beaufort Sea: Mean structure and  
924 variability. *Journal of Geophysical Research C: Oceans*, 109, 1-14.  
925 <https://doi.org/10.1029/2003JC001912>.

926 Pickart, R. S., Weingartner, T. J., Pratt, L. J., Zimmermann, S. & Torres, D. J. (2005). Flow of  
927 winter-transformed Pacific water into the Western Arctic. *Deep-Sea Research Part II:*  
928 *Topical Studies in Oceanography*, 52, 3175-3198.  
929 <https://doi.org/10.1016/j.dsr2.2005.10.009>.

930 Poirier, R. K., Cronin, T. M., Briggs, W. M. & Lockwood, R. (2012). Central Arctic  
931 paleoceanography for the last 50kyr based on ostracode faunal assemblages. *Marine*  
932 *Micropaleontology*, 88-89, 65-76. <https://doi.org/10.1016/j.marmicro.2012.03.004>.

933 Polyak, L., Belt, S.T., Cabedo-Sanz, P., Yamamoto, M., Park, Y.-H. (2016). Holocene sea-ice  
934 conditions and circulation at the Chukchi-Alaskan margin, Arctic Ocean, inferred from  
935 biomarker proxies. *The Holocene* 26, 1810–1821.

936 Polyakov, I. V., Pnyushkov, A. V., Alkire, M. B., Ashik, I. M., Baumann, T. M., Carmack, E. C.,  
937 Goszczko, I., Guthrie, J., Ivanov, V. V., Kanzow, T., Krishfield, R., Kwok, R., Sundfjord,  
938 A., Morison, J., Rember, R. & Yulin, A. (2017). Greater role for Atlantic inflows on sea-  
939 ice loss in the Eurasian Basin of the Arctic Ocean. *Science*, 356, 285-291.  
940 <https://doi.org/10.1126/science.aai8204>.

941 Porcelli, D., Andersson, P. S., Baskaran, M., Frank, M., Björk, G. & Semiletov, I. (2009). The  
942 distribution of neodymium isotopes in Arctic Ocean basins. *Geochimica et Cosmochimica*  
943 *Acta*, 73, 2645-2659. <https://doi.org/10.1016/j.gca.2008.11.046>.

944 Rickli, J., Frank, M., Baker, A. R., Aciego, S., de Souza, G., Georg, R. B. & Halliday, A. N.  
945 (2010). Hafnium and neodymium isotopes in surface waters of the eastern Atlantic Ocean:  
946 Implications for sources and inputs of trace metals to the ocean. *Geochimica et*  
947 *Cosmochimica Acta*, 74, 540-557. <https://doi.org/10.1016/j.gca.2009.10.006>.

948 Rickli, J., Frank, M. & Halliday, A. N. (2009). The hafnium–neodymium isotopic composition of  
949 Atlantic seawater. *Earth and Planetary Science Letters*, 280, 118-127.  
950 <https://doi.org/10.1016/j.epsl.2009.01.026>.

951 Rudels, B. (2012). Arctic Ocean circulation and variability - advection and external forcing  
952 encounter constraints and local processes. *Ocean Science*, 8, 261-286.  
953 <https://doi.org/10.5194/os-8-261-2012>

- 954 Rudels, B., Jones, E. P., Schauer, U. & Eriksson, P. (2004). Atlantic Sources of the Arctic Ocean  
955 Halocline. *Polar Research*, 23, 181-208. <https://doi.org/10.1111/j.1751-8369.2004.tb00007.x>.
- 957 Schoster, F., Behrends, M., Muller, R., Stein, R. & Washner, M. (2000). Modern river discharge  
958 and pathways of supplied material in the Eurasian Arctic Ocean: Evidence from mineral  
959 assemblages and major and minor element distribution. *International Journal of Earth  
960 Sciences*, 89, 486-495. <https://doi.org/10.1007/s005310000120>.
- 961 Serreze, M. C., Holland, M. M. & Stroeve, J. (2007). Perspectives on the Arctic's Shrinking Sea-  
962 Ice Cover. *Science*, 315, 1533-1536. <https://doi.org/10.1126/science.1139426>.
- 963 Screen, J.A. and Francis, J.A. (2016). Contribution of sea-ice loss to Arctic amplification is  
964 regulated by Pacific Ocean decadal variability. *Nature Climate Change* 6, 856–860.
- 965 Shimada, K., Kamoshida, T., Itoh, M., Nishino, S., Carmack, E., McLaughlin, F., Zimmermann,  
966 S. & Proshutinsky, A. (2006). Pacific Ocean inflow: Influence on catastrophic reduction  
967 of sea ice cover in the Arctic Ocean. *Geophysical Research Letters*, 33, 3-6.  
968 <https://doi.org/10.1029/2005GL025624>.
- 969 Stein, R., Fahl, K., Schade, I., Manerung, A., Wassmuth, S., Niessen, F. & Nam, S.-I. (2017).  
970 Holocene variability in sea ice cover, primary production, and Pacific-Water inflow and  
971 climate change in the Chukchi and East Siberian Seas (Arctic Ocean). *Journal of  
972 Quaternary Science*, 32, 362-379. <https://doi.org/10.1002/jqs.2929>.
- 973 Stichel, T., Frank, M., Rickli, J. & Haley, B. A. (2012). The hafnium and neodymium isotope  
974 composition of seawater in the Atlantic sector of the Southern Ocean. *Earth and  
975 Planetary Science Letters*, 317-318, 282-294. <https://doi.org/10.1016/j.epsl.2011.11.025>.
- 976 Tachikawa, K., Jeandel, C., Vangriesheim, A. & Dupré, B. (1999). Distribution of rare earth  
977 elements and neodymium isotopes in suspended particles of the tropical Atlantic Ocean  
978 (EUMELI site). *Deep-Sea Research Part I: Oceanographic Research Papers*, 46, 733-  
979 755. [https://doi.org/10.1016/S0967-0637\(98\)00089-2](https://doi.org/10.1016/S0967-0637(98)00089-2).
- 980 Taylor, S. R. & McClennan, S. M. 1985: *The continental crust: Its composition and evolution*.  
981 312-312 pp. John Wiley & Sons Ltd, Oxford.
- 982 VanLaningham, S., Pisias, N.G., Duncan, R.A., and Clift, P.D., 2009. Glacial–interglacial  
983 sediment transport to the Meiji Drift, northwest Pacific Ocean: evidence for timing of  
984 Beringian outwashing. *Earth Planet. Sci. Lett.*, 277(1–2):64–72.
- 985 Vervoort, J. D., Patchett, P. J., Blichert-toft, J. & Albare, F. (1999). Relationships between Lu –  
986 Hf and Sm – Nd isotopic systems in the global sedimentary system. *Earth and Planetary  
987 Science Letters*, 168, 79-99. [https://doi.org/10.1016/S0012-821X\(99\)00047-3](https://doi.org/10.1016/S0012-821X(99)00047-3).
- 988 Wagner, A., Lohmann, G. & Prange, M. (2011). Arctic river discharge trends since 7ka BP.  
989 *Global and Planetary Change*, 79, 48-60.  
990 <https://doi.org/10.1016/j.gloplacha.2011.07.006>.
- 991 Wahsner, M., Müller, C., Stein, R., Ivanov, G., Levitan, M., Shelekhova, E. & Tarasov, G.  
992 (1999). Clay-mineral distribution in surface sediments of the Eurasian Arctic Ocean and  
993 continental margin as indicator for source areas and transport pathways - a synthesis.  
994 *Boreas*, 28, 215-233. <https://doi.org/10.1111/j.1502-3885.1999.tb00216.x>.
- 995 Wanner, H., Beer, J., Bütikofer, J., Crowley, T. J., Cubasch, U., Flückiger, J., Goosse, H.,  
996 Grosjean, M., Joos, F., Kaplan, J. O., Küttel, M., Müller, S. A., Prentice, I. C., Solomina,  
997 O., Stocker, T. F., Tarasov, P., Wagner, M. & Widmann, M. (2008). Mid- to Late  
998 Holocene climate change: an overview. *Quaternary Science Reviews*, 27, 1791-1828.  
999 <https://doi.org/10.1016/j.quascirev.2008.06.013>.

- 1000 Weingartner, T., Aagaard, K., Woodgate, R., Danielson, S., Sasaki, Y. & Cavalieri, D. (2005).  
1001 Circulation on the north central Chukchi Sea shelf. *Deep Sea Research Part II: Topical*  
1002 *Studies in Oceanography*, 52, 3150-3174. <https://doi.org/10.1016/j.dsr2.2005.10.015>.
- 1003 Weis, D., Kieffer, B., Maerschalk, C., Barling, J., De Jong, J., Williams, G. A., Hanano, D.,  
1004 Pretorius, W., Mattielli, N., Scoates, J. S., Goolaerts, A., Friedman, R. M. & Mahoney, J.  
1005 B. (2006). High-precision isotopic characterization of USGS reference materials by TIMS  
1006 and MC-ICP-MS. *Geochemistry, Geophysics, Geosystems*, 7.  
1007 <https://doi.org/10.1029/2006GC001283>.
- 1008 Wickert, A. D. (2016). Reconstruction of North American drainage basins and river discharge  
1009 since the Last Glacial Maximum. *Earth Surface Dynamics*, 4, 831-869.  
1010 <http://dx.doi.org/10.5194/esurf-2016-8>.
- 1011 Wilson, D.J., Piotrowski, A.M., Galy, A., & Clegg, J.A. (2013). Reactivity of neodymium  
1012 carriers in deep sea sediments: Implications for boundary exchange and  
1013 paleoceanography. *Geochimica et Cosmochimica Acta*, 109, 197–221.  
1014 [doi:10.1016/j.gca.2013.01.042](https://doi.org/10.1016/j.gca.2013.01.042)
- 1015 Winsor, P. and Chapman, D.C. (2004). Pathways of Pacific water across the Chukchi Sea: A  
1016 numerical model study. *Journal of Geophysical Research* 109:  
1017 C03002.[doi:10.1029/2003JC001962](https://doi.org/10.1029/2003JC001962).
- 1018 Woodgate, R. A., Aagaard, K., Swift, J. H., Falkner, K. K. & Smethie, W. M. (2005). Pacific  
1019 ventilation of the Arctic Ocean's lower halocline by upwelling and diapycnal mixing over  
1020 the continental margin. *Geophysical Research Letters*, 32, 1-5.  
1021 <https://doi.org/10.1029/2005GL023999>.
- 1022 Yamamoto, M., Nam, S.-I., Polyak, L., Kobayashi, D., Suzuki, K., Irino, T. & Shimada, K.  
1023 (2017). Holocene dynamics in the Bering Strait inflow to the Arctic and the Beaufort  
1024 Gyre circulation based on sedimentary records from the Chukchi Sea. *Climate of the Past*,  
1025 13, 1111-1127. <https://doi.org/10.5194/cp-13-1111-2017>.
- 1026 Zimmermann, B., Porcelli, D., Frank, M., Andersson, P. S., Baskaran, M., Lee, D.-C. & Halliday,  
1027 A. N. (2009a). Hafnium isotopes in Arctic Ocean water. *Geochimica et Cosmochimica*  
1028 *Acta*, 73, 3218-3233. <https://doi.org/10.1016/j.gca.2009.02.028>.
- 1029 Zimmermann, B., Porcelli, D., Frank, M., Rickli, J., Lee, D.-C. & Halliday, A. N. (2009b). The  
1030 hafnium isotope composition of Pacific Ocean water. *Geochimica et Cosmochimica Acta*,  
1031 73, 91-101. <https://doi.org/10.1016/j.gca.2008.09.033>.
- 1032

## 1033 **Figure captions**

1034 **Figure 1.** (a) Schematic map of Atlantic water (AW), Pacific water (PW), Transpolar Drift (TPD)  
1035 and Beaufort Gyre (BG) circulation in the Arctic Ocean and locations of cores 01JPC and 02PC  
1036 (black circles). The PW drifts eastward in the Beaufort Sea and is known as the Alaskan Coastal  
1037 Current (ACC). The  $\epsilon\text{Nd}$  and  $\epsilon\text{Hf}$  values are shown in the map. The Laurentide Ice Sheet at 11.5  
1038 ka cal BP is also shown (Dyke, 2004). (b) East-west mean annual temperature profile across the  
1039 Beaufort-Chukchi slope (transect 1-2 in gray). Core sites are marked by black circles.  
1040 Temperature data are from Polar Science Center Hydrographic Climatology (PHC,  
1041 <http://psc.apl.washington.edu/Climatology.html>).  
1042

1043 **Figure 2.** REE patterns normalized to PAAS (Taylor & McClelland, 1985) for the bulk sediment  
1044 leachate samples from (a) core 01JPC (Chukchi-Alaskan margin) and (b) core 02PC (Canadian  
1045 Beaufort margin).  
1046

1047 **Figure 3.** (a)  $^{87}\text{Sr}/^{86}\text{Sr}$  isotope ratios for the bulk sediment leachate samples from cores 01JPC  
1048 and 02PC; sea water values in the Arctic ocean are shown by the black lines (Asahara et al.,  
1049 2012). (b) Cross-plot of HREE/LREE vs. MREE. A mixing line between the most  
1050 MREE-enriched leachates and the most HREE-enriched oxic pore waters reflects the authigenic-  
1051 pore water array (Gutjahr et al., 2010). Detrital REE composition of cores 02PC and 05JPC are  
1052 from Deschamps (2018). (c) Spearman correlation between  $\Sigma\text{REE}$  contents and the authigenic  
1053  $\epsilon\text{Nd}$  values from cores 01JPC and 02PC. (d) Hafnium–neodymium isotope systematics of the  
1054 bulk sediment leachates obtained in this study together with previously published data and  $\epsilon\text{Nd}$ -  
1055  $\epsilon\text{Hf}$  correlation lines from the literature. Terrestrial and seawater arrays are from Vervoort et al.  
1056 (1999) and Albarède et al. (1998), respectively. Pacific water, Mackenzie River and Arctic Sea  
1057 water values are from Zimmermann et al. (2009a,b), and leachate and detrital values are from  
1058 Chen et al. (2012).  
1059

1060 **Figure 4.** Nd and Hf isotopic evolution of the Arctic deep-waters obtained from cores 02PC and  
1061 01JPC. Horizontal blue and red lines illustrate modern values of the Bering Sea Water  
1062 (Zimmermann et al., 2009a,b; Asahara et al., 2012; Jang et al., 2017), Atlantic water and  
1063 Mackenzie River (Porcelli et al., 2009; Zimmermann et al., 2009a). The green arrows indicate the  
1064 more unradiogenic Nd isotope compositions from the Alaskan Coastal Water (VanLaningham et  
1065 al., 2009; Horikawa et al., 2010, 2015) and the geological terrains of the Canadian Arctic  
1066 Archipelago (CAA; Maccali et al., 2018).  
1067

1068 **Figure 5.** On the left: (a) Mean summer insolation at  $70^\circ\text{N}$  (Berger & Loutre, 1991); (b) Global  
1069 sea level curve (RSL; Lambeck et al., 2014); (c) Authigenic  $\epsilon\text{Nd}$  records of a sediment core from  
1070 the Fram Strait (Maccali et al., 2013); (d) Holocene  $\delta^{18}\text{O}$  records from Jellybean Lake used as a  
1071 PDO index (Barron & Anderson, 2011); (e) Holocene Mackenzie River discharge based on  
1072 numerical models (Wagner et al., 2011); (f) Dinocyst-based reconstructions of sea ice cover from  
1073 the Canadian Beaufort Sea (Bringué and Rochon, 2012); (g) Proportion of sediment from the  
1074 Mackenzie River (black) and the Canadian Arctic Archipelago (CAA; red) in core 02PC  
1075 (Deschamps et al., 2018a); (h-i) Authigenic  $\epsilon\text{Nd}$  and  $\epsilon\text{Hf}$  evolution for core 02PC (this study). On  
1076 the right: schematic illustrations depicting the changes in authigenic  $\epsilon\text{Nd}$  and  $\epsilon\text{Hf}$  variations in  
1077 core 02PC between (j) 12 and 8 ka cal BP (light blue), (k) 8 and 4 ka cal BP (white), and (l) after  
1078 4 cal ka BP (light red). Spirals indicate sediment resuspension on the Canadian Beaufort slope  
1079 (Osborne and Forest, 2016).  
1080

1081 **Figure 6.** On the left: (a) Mean summer insolation at  $70^\circ\text{N}$  (Berger & Loutre, 1991); (b)  
1082 Holocene  $\delta^{18}\text{O}$  records from Jellybean Lake used as a PDO index (Barron & Anderson, 2011); (c)  
1083 sea ice proxy PIP25 (based on brassicasterol) from core ARA2B-1A (Stein et al., 2017); (d)  
1084 Quantitative reconstruction of past sea surface temperature (red) and sea-ice cover (blue) in the  
1085 core 05JPC based on dinoflagellate cyst assemblages (McKay et al., 2008); (e) Authigenic  $\epsilon\text{Nd}$   
1086 evolution for core 01JPC (this study); (f) Proportion of northeastern Bering Sea sediments (this  
1087 study); (g)  $\text{Log}(\text{I}+\text{K}/\text{C}+\text{V})$  ratio in core 01JPC; (h) Amorphous silica content in core 01JPC (this

1088 study). On the right: (i-j) schematic illustrations depicting the changes in authigenic  $\epsilon\text{Nd}$   
1089 variations in core 01JPC before 4 cal ka BP (light blue) and after 4 ka cal BP (light red). Spirals  
1090 indicate possible sediment resuspension on the Chukchi-Alaskan slope (Darby et al., 2009).

1091  
1092 **Figure 7.** Generalized reconstructions showing the possible changes in the Pacific Water inflow  
1093 into the western Arctic Ocean during the Holocene (modified from Grebmeier et al., 2006)  
1094 inferred from the authigenic  $\epsilon\text{Nd}$  records of cores 01JPC and 02PC. The Laurentide Ice Sheet  
1095 position in (a) is about of 11.5 ka cal BP (Dyke, 2004). The Aleutian Low (the bold AL in b and  
1096 c) patterns according to the PDO-like conditions are also show (Anderson et al., 2016). AR:  
1097 Anadyr River, YR:Yukon River, MR: Mackenzie River, BG: Beaufort Gyre, AG: Amundsen  
1098 Gulf.  
1099

## 1100 **Supplementary material**

1101 **Figure S1.**  $\text{Fe}/k_{\text{LF}}$  and  $\text{Mn}/\text{Ti}$  ratios for cores 01JPC and 02PC (data from Deschamps et al.,  
1102 2018b). The mean  $\text{Fe}/k_{\text{LF}}$  ratio in cores 01JPC and 02PC is  $<40$  Mcps, suggesting weak  
1103 reductive diagenesis (Funk, 2004; Hofmann et al., 2005; Hofmann & Fabian, 2009). Moreover,  
1104 the vertical distribution of the  $\text{Mn}/\text{Ti}$  ratio shows little variability within the studied cores, with  
1105 elevated ratios recorded towards the top of the cores. These elevated values demonstrate  
1106 scavenging of  $\text{Mn}/\text{Fe}$  oxyhydroxides and associated trace metals from the water column (e.g.,  
1107 Macdonald and Gobeil, 2012; Meinhardt et al., 2016b).

1108  
1109 **Figure S2.**  $\epsilon\text{Hf}$  signature of core 01JPC. Horizontal blue and red lines illustrate modern values of  
1110 the North Pacific water. Due to the large uncertainties, the  $\epsilon\text{Hf}$  signature of core 01JPC cannot be  
1111 used to observe Holocene changes in the  $\epsilon\text{Hf}$  Pacific signature.

1112  
1113 **Table S1.** REE and trace element concentrations (ppm) from bulk sediment leachates of cores  
1114 01JPC and 02PC.

1115  
1116 **Table S2.** Nd-Hf-Sr isotopes from bulk sediment leachates of cores 01JPC and 02PC.

1117  
1118 **Table S3.** Bulk minerals data from core 01JPC used in this study (all values given in %).

1119  
1120 **Table S4.** Clay minerals data from core 01JPC used in this study (all values given in %). ND: not  
1121 detected.

1122  
1123 **Table S5.** SedUnMixMC results from core 01JPC. Source 1: Mackenzie River plume (Gamboa et  
1124 al., 2017); Source 2: North Alaska (Darby et al., 2011); Source 3: Banks and Victoria Island  
1125 (Gamboa et al., 2017; this study); Source 4: Bearing Strait (Stein et al., 2017); Source 5: East  
1126 Siberian Sea & Laptev Sea (Darby et al., 2011); Source 6: Kara Sea (Andrews et al. 2016).

Figure 1.

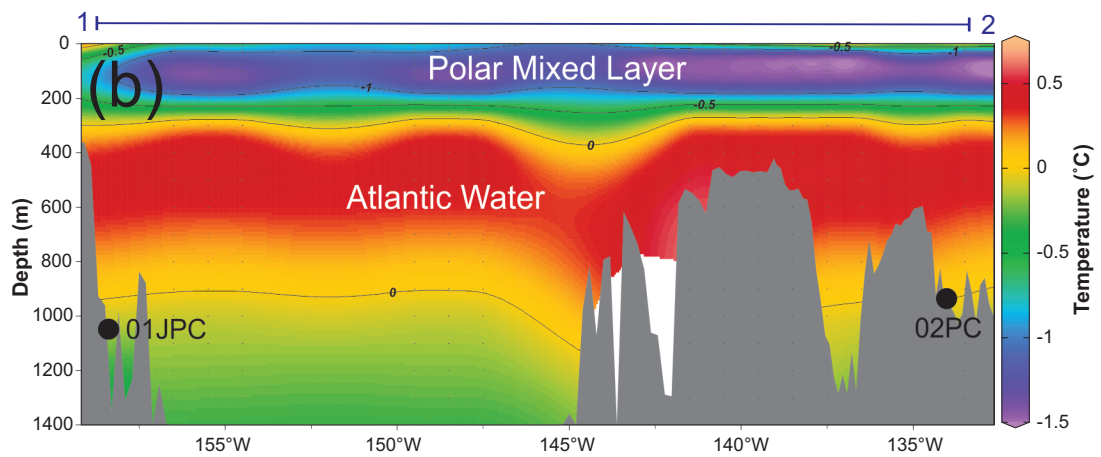
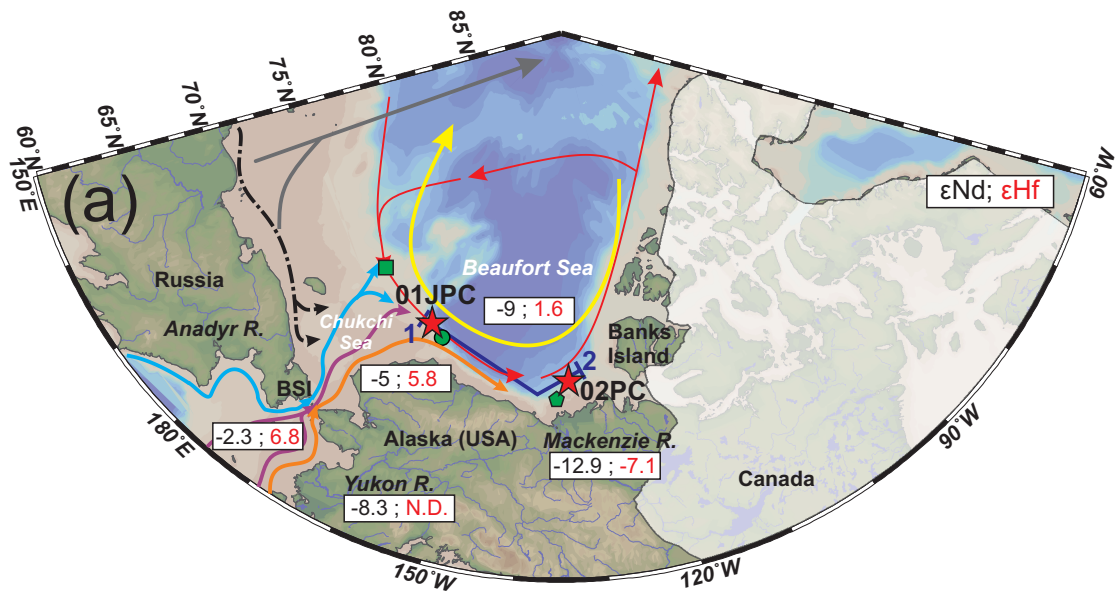


Figure 2.

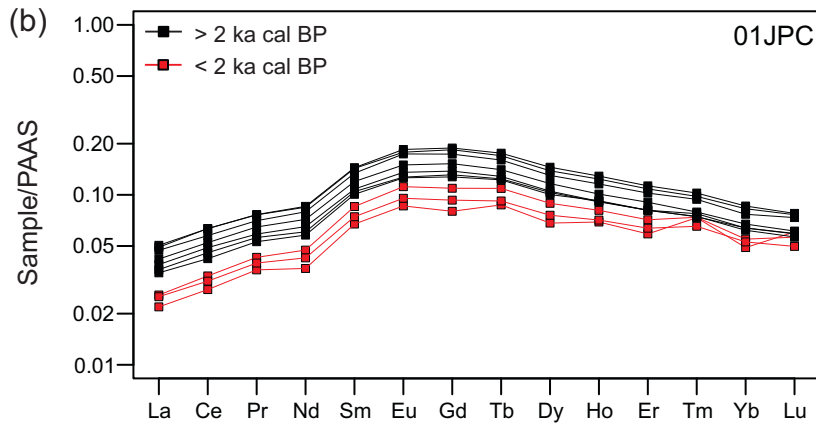
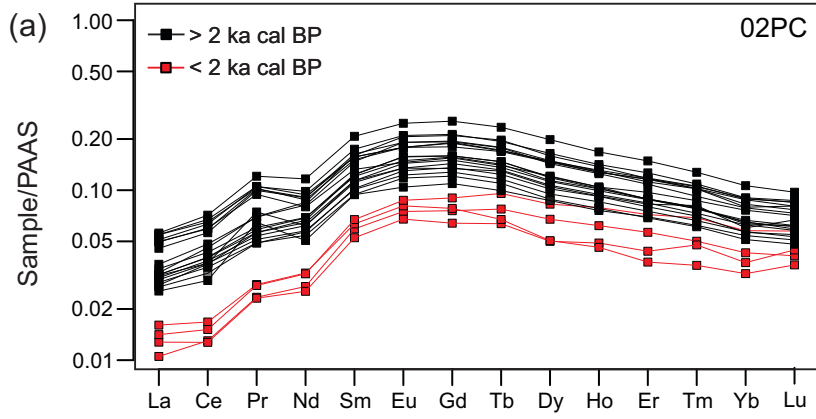
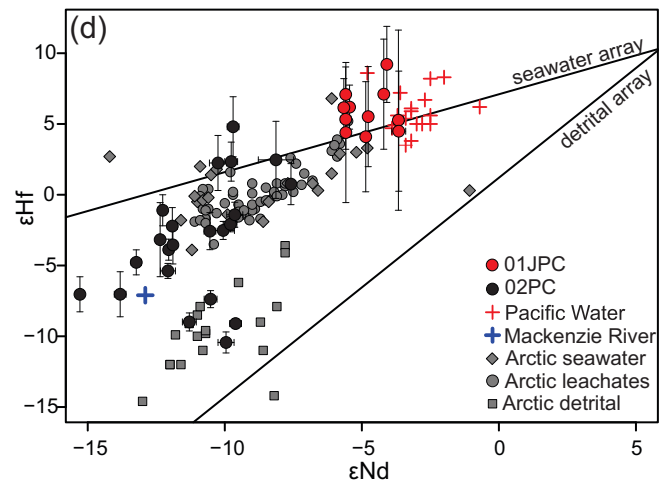
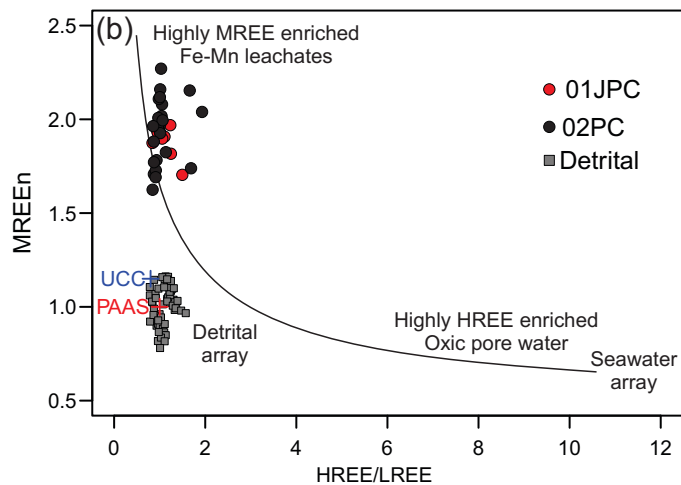
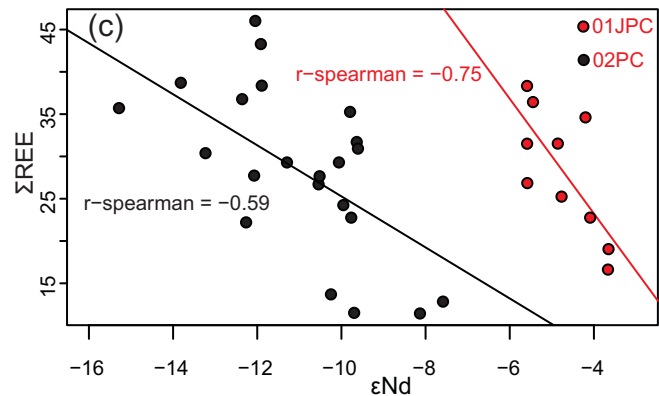
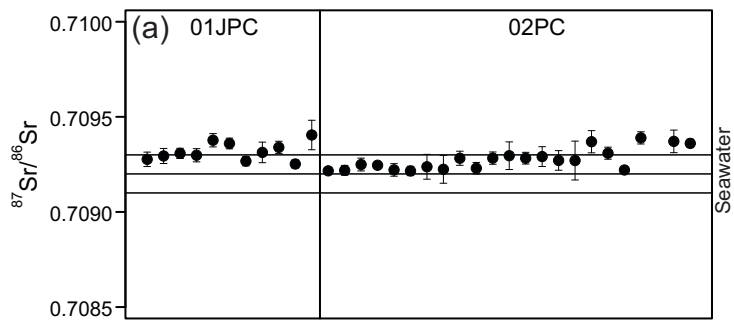


Figure 3.



**Figure 4.**

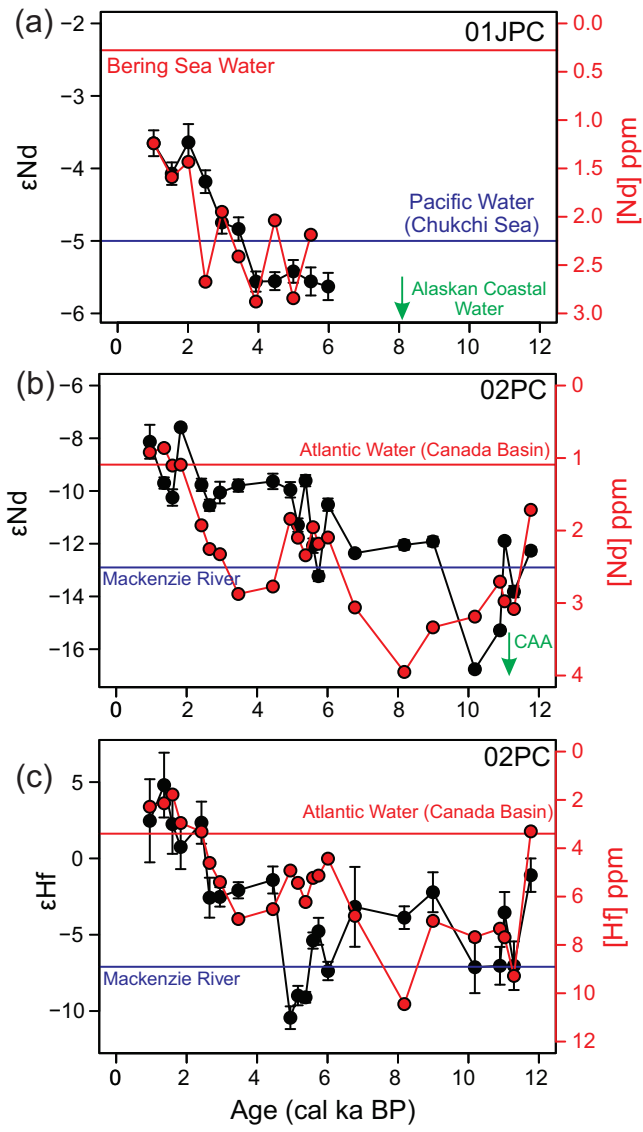


Figure 5.

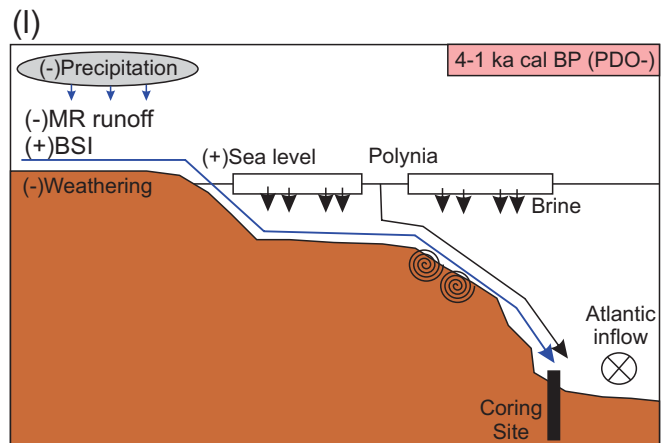
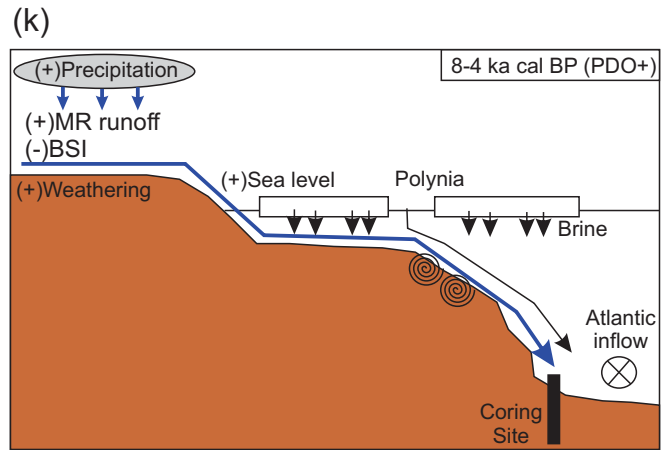
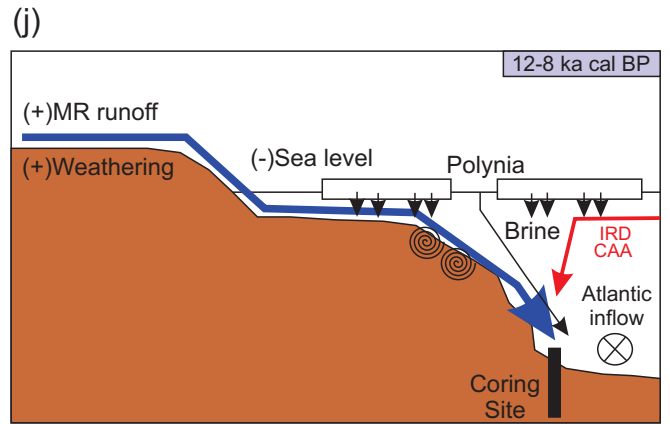
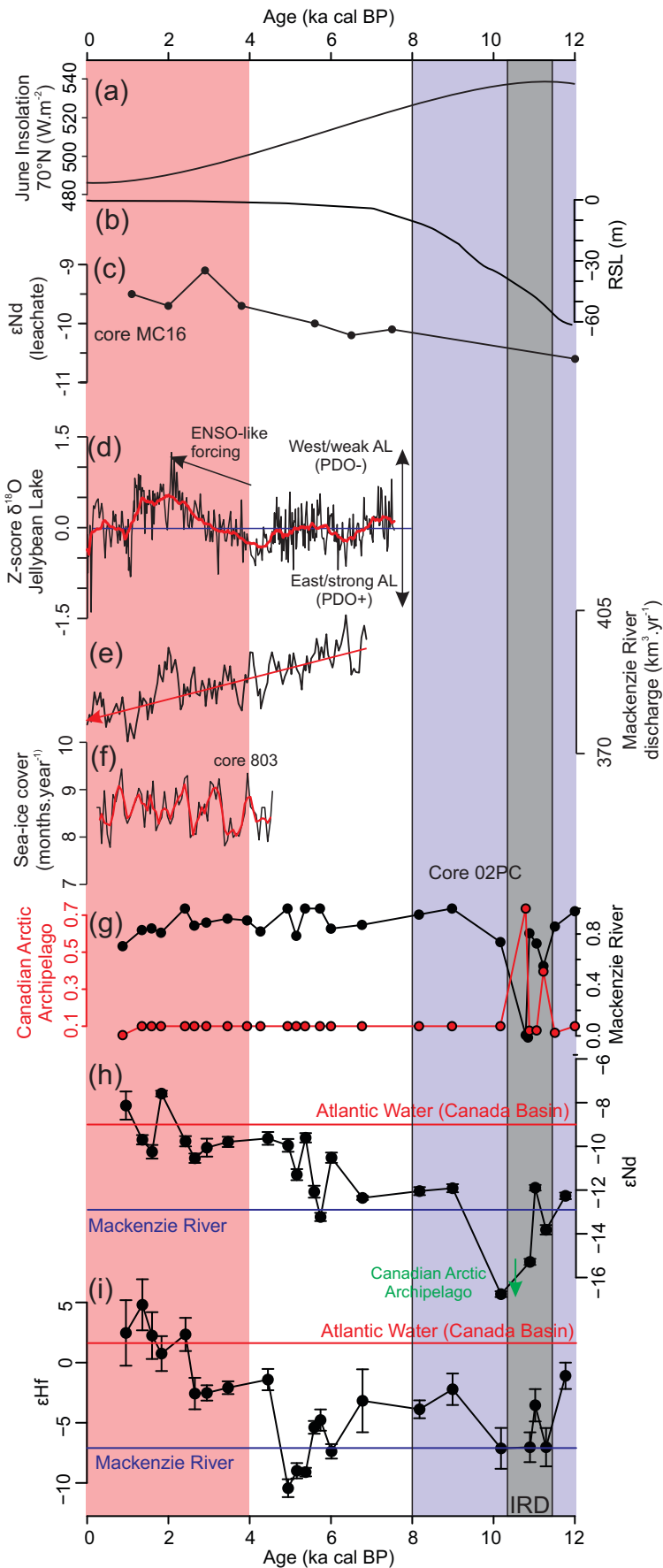


Figure 6.

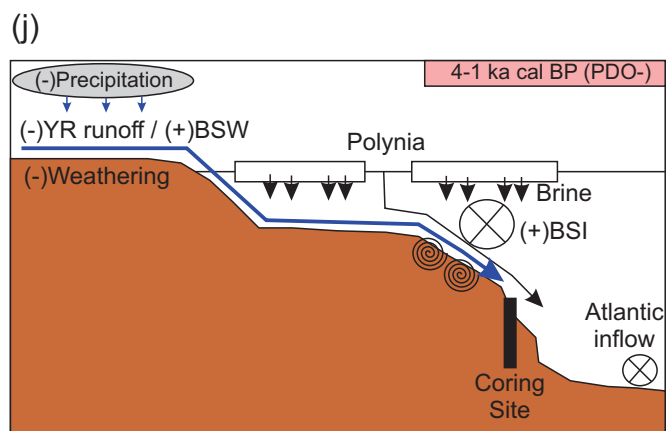
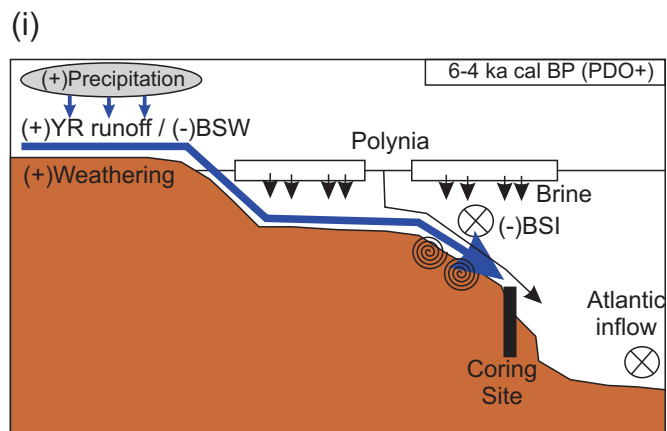
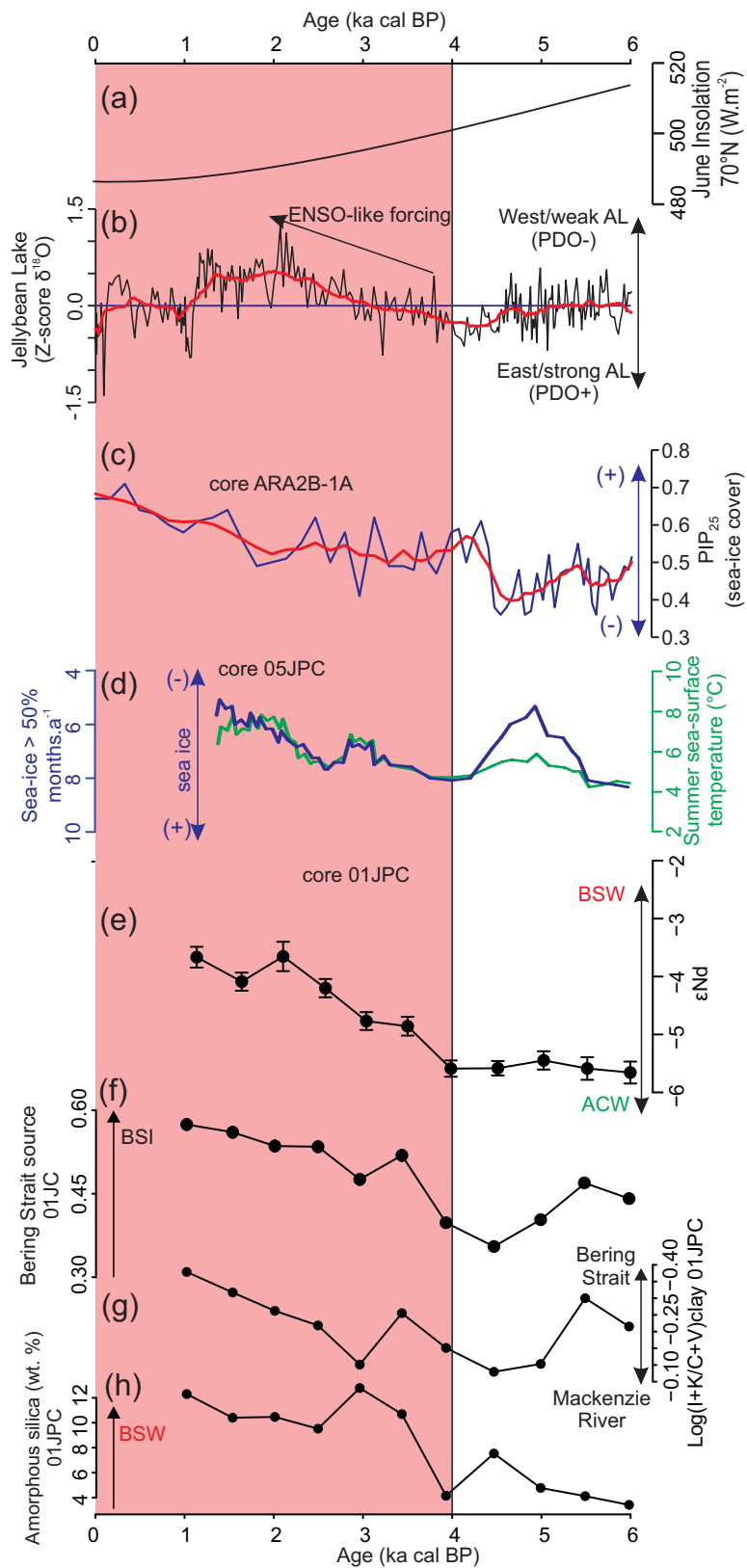
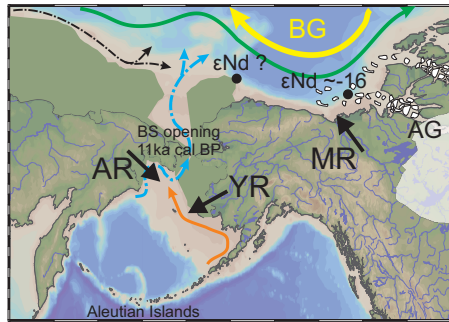
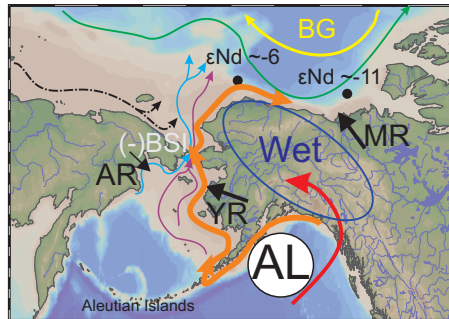


Figure 7.

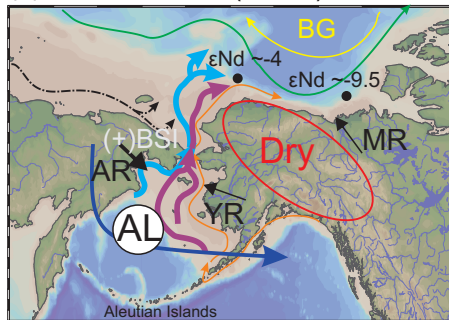
(a) 12-10 ka cal BP



(b) 8-4 ka cal BP (PDO+)



(c) 4-1 ka cal BP (PDO-)



Legend	
<span style="color: yellow;">—</span>	Beaufort Gyre (surface)
<span style="color: green;">—</span>	Atlantic Water (subsurface)
<span style="color: black;">- - -</span>	Siberian Coastal Current
<span style="color: orange;">—</span>	Alaska Coastal Water
<span style="color: purple;">—</span>	Bering Shelf Water
<span style="color: blue;">—</span>	Anadyr Water
	] Bering Sea Water